npj | 2D Materials and Applications

www.nature.com/npj2dmaterials

REVIEW ARTICLE OPEN

Check for updates

# Photoluminescence as a probe of phosphorene properties

Maciej R. Molas[1], Łukasz Macewicz[2], Aleksandra Wieloszyńska[2], Paweł Jakóbczyk[2], Andrzej Wysmołek[1], Robert Bogdanowicz[2]✉ and Jacek B. Jasinski[3]✉

Here, we provide a detailed evaluation of photoluminescence (PL) as a comprehensive tool for phosphorene characterization with the emphasis on a prominent quantitative role of PL in providing fingerprint-like features due to its extreme sensitivity to the band structure details, anisotropy, disorder, external fields, etc. Factors such as number of layers, dimensionality, structural and chemical disorder, and environmental factors and their effect on phosphorene's PL signal are reviewed and discussed. Applications of PL in monitoring phosphorene and its modifications, as well as potential impacts on the fields of chemical and biosensing, nanomedicine, and solar energy harvesting, are also elaborated.

*npj 2D Materials and Applications* (2021)5:83 ; https://doi.org/10.1038/s41699-021-00263-8

## INTRODUCTION

Since December of 2013, when two groups independently reported using adhesive tape for the successful isolation of 2–3 atomic layers of bulk black phosphorus (BP)[1–3], the two-dimensional (2D) form of BP, phosphorene, has attracted a lot of scientific attention, both in terms of fundamental research, as well as exciting potential applications. Phosphorene's combination of properties, such as a layer-dependent and highly tunable bandgap between 0.3 and 2 eV, intrinsic p-type conductivity with high carrier mobility up to 1000 $cm^2 V^{-1} s^{-1}$, highly anisotropic structure and properties, Peierls distortion, and inter alia superconductivity are attracting a growing number of studies by researchers from various disciplines.

BP is an orthorhombic layered allotrope of phosphorous, featuring layers of corrugated six-membered rings[4]. Phosphorene, a single layer of BP, has a puckered honeycomb structure with two drastically different crystallographic directions, the so-called zigzag (ZZ) and armchair (AC) directions. A schematic showing the atomic structure of three layers of BP along with a diagram depicting processes associated with the light absorption and emission in BP is shown in Fig. 1. The strong in-plane anisotropy of phosphorene is reflected in its strong anisotropy of electronic band structure and optical properties, which together with its high carrier mobility make phosphorene a highly promising 2D material for a wide range of applications ranging from electronic, spintronic, and optoelectronic devices to sensors, thermoelectric, and batteries. The π–Σ interaction in phosphorene is weaker than the π–π interaction in a competitive graphene (phosphorene—0.086 kcal $mol^{-1}$; graphene—0.400 kcal $mol^{-1}$)[5,6]. While the charge carrier mobilities in phosphorene are comparable to those in a ML of $MoS_2$, being a single-element material, phosphorene can, at least potentially, be fabricated at higher purity.

Although the most stable among phosphorus allotropes, when in a 2D form, BP shows high reactivity. This allows for easy surface functionalization and tailoring properties of phosphorene through chemical modifications. In particular, phosphorene can be chemically modified by both adsorption and covalent fashions. The reactions rates or charge transfer between various molecules and phosphorene show large (1–3 orders of magnitude) anisotropy along different directions, which is consistent with the anisotropy of the electronic band structure of this material[6–9]. It is noteworthy that the anisotropic pathways of chemical interactions or defect-induced variations of energy band structure can be used to tune the phosphorene electronic and optical response.

One of the most important properties of phosphorene is a thickness-dependent tunable bandgap ranging from 2 eV for a ML to 0.3 eV for bulk material[10]. Such a wide bandgap variability along with additional tuning capabilities by using chemical functionalization, defect and/or strain engineering, external electric field, etc. make phosphorene especially attractive for optoelectronic applications in the visible and infrared (IR) spectral range, such as solar energy harvesting, photocatalysis, photodetection, etc. In addition to its widely tunable bandgap, phosphorene can be switched between insulating and conducting states by substitutional or surface doping. Wang et al.[11] have shown that adatoms of boron, carbon, nitrogen, oxygen, and fluorine act as impurities and induce mid-gap states leading to a metallic characteristic of phosphorene. High tunability of electrical properties, together with sufficiently flat morphology to confine electrons and facilitate high carrier mobility, makes phosphorene an interesting material for sensing applications, such as organic biosensors and implanted devices for reading life functions or vital signals.

A high reactivity makes phosphorene also highly sensitive to its environment and prone to ambient degradation. The poor environmental stability is a major hurdle limiting diverse applications and fundamental studies of this material. Understanding the degradation mechanism and developing strategies to circumvent this process has therefore become an intense area of research[12–16].

While several factors such as exposure to water and air or illumination with light have been suspected to affect the stability of BP, several recent systematic studies have shown that oxygen plays a crucial role in modifying the surface of this material. Dissociative chemisorption of $O_2$ that leads to the decomposition of BP has been found to be the main mechanism responsible for the oxidation of BP surface. During this process, changes in the electronic structure along with modifications of the surface properties take place. Contact angle measurements have shown that the hydrophobic surface of pristine BP gradually becomes hydrophilic upon oxidation[12]. When oxidation takes place in presence of water, phosphoric acid species are formed on BP

[1]Institute of Experimental Physics, Faculty of Physics, University of Warsaw, Warsaw, Poland. [2]Gdańsk University of Technology, Gdańsk, Poland. [3]Conn Center for Renewable Energy Research, University of Louisville, Louisville, KY 40292, USA. ✉email: rbogdan@eti.pg.edu.pl; jacek.jasinski@louisville.edu

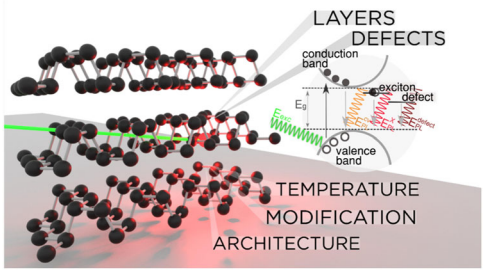


**Fig. 1 Photoluminescence of phosphorene.** A schematic diagram depicting origin of emission and factors affecting PL signal in phosphorene.

surface, which in turn lead to increased oxidation[12]. Notably, water in absence of $O_2$ has negligible effects on BP surface[12]. In fact, stable dispersion of exfoliated BP in deaerated (i.e., $O_2$ depleted) water can be obtained and stored in inert gas atmosphere without any noticeable degradation[12,17]. It has been shown that pure oxygen produces an oxide layer on the BP surface while oxidation in water takes place preferentially at the defects such as edges or steps[16]. Illumination has been found to accelerate BP oxidation[13,15,16,18] with a strong flake thickness-dependent degradation rate[13]. BP can be also effectively modified or processed using etching. Island et al.[19] have reported that BP flakes are etched into the air or defected by the physisorption of oxygen and nitrogen in just minutes. Hu and Yang[20] have calculated the stability of phosphorene and its electronic structure versus typical point defects. They have revealed that defects common for graphene and silicene such as a Stone–Wales defect and single and double vacancies are also present in phosphorene. Ziletti et al.[21] have shown that the formation of oxygen-related defects in phosphorene is caused by oxygen chemisorption.

The most common methods to fabricate phosphorene from BP are various top-down techniques of separating a single of a few atomic layers from a bulk precursor through exfoliation (shown in Fig. 2)[22]. Layered materials (LMs) exhibit strong in-plane chemical bonds but rather weak out-of-plane, van der Waals (vdW) bonds, enabling the exfoliation process. In the first studies on the successful fabrication of phosphorene, mechanical exfoliation was utilized to separate few-layer flakes down to single sheets[23] by applying blue Nitto tape followed by pilling off layers on a polydimethylsiloxane substrate (see Fig. 2a). Later on, Brent et al.[24] produced few-layer phosphorene by liquid exfoliation of BP in N-methyl-2-pyrrolidone (NMP) using an ultrasonic bath, as depicted in Fig. 2b. The liquid exfoliation method enables the production of phosphorene flakes which are stable in water[25] thanks to the $OH^-$ adsorbed at the surface by adding NaOH during sonication. The influence of a specific solvent on the exfoliation of BP was surveyed by Yasaei et al.[26]. They revealed that aprotic and polar solvents (e.g., dimethylformamide (DMF) or dimethyl sulfoxide) favor stability of phosphorene dispersions. Kumar[27] manifested that the combination of aprotic solvent with ionic sulfonated polymer (Nafion) could be utilized for simultaneous exfoliation and passivation of phosphorene nanosheets causing additionally their morphological transformation (i.e., nanoribbons).

Stable aqueous phosphorene dispersions of optically and electronically active phosphorene can also be produced using a method based on surfactant-assisted exfoliation and postprocessing of BP in deoxygenated water[17]. Furthermore, Lu et al.[28] developed a method of fabricating ML phosphorene using a plasma-assisted technique. The method includes cleaving of few-layer phosphorene onto $Si/SiO_2$ substrates, as displayed in Fig. 2c, followed by thinning using argon plasma. The process can be done at room temperature and is fast (20 s thinning using a 13.56 MHz RF plasma source was shown to be effective). Optionally, chemical vapor transport can be used with red phosphorus as a precursor to grow single crystals of BP in several millimeter sizes[4]. Such crystals can be used for the fabrication of single- or multilayer high area phosphorene samples. Recently, 1064 nm laser-assisted crystallization of phosphorene layers from red phosphorus was reported by Rajabali et al.[29]. Figure 2d shows the transformation process that happens in the subsequent sequence of atmosphere switching between argon–oxygen (Ar:$O_2$) and helium–hydrogen (He:$H_2$) mixtures. Also recently, Erande et al.[30] demonstrated an electrochemical method capable of producing phosphorene nanosheets. In this method, the BP crystal is utilized as the working electrode and immersed in 0.5 M $Na_2SO_4$, while a platinum wire is used as the counter electrode. The process is carried out by applying a positive bias voltage of about +7 V and a current of 0.2 A (see Fig. 2e). Application of plasma–liquid exfoliation allows for 10 nm in-depth resolution along with ultrashort times of 5 min. Uniform BP flake isolation in DMF[31] can be obtained by applying a high voltage of 2 kV at a BP cathode as presented in Fig. 2f.

Optical spectroscopy has been shown to be an effective approach to characterize the material's quality and to probe the structure and property changes in phosphorene samples. Lan et al.[32,33] reported intensive light–phosphorene interactions in the mid-IR range manifested by anisotropic absorption behavior. It has been shown[34,35] that the nonlinear saturable absorption performance of phosphorene is stronger than that of $MoS_2$, $WS_2$, or graphene in a wide spectral range. Surprisingly, few-layer BP (FLBP) exhibits the enhanced frequency-integrated exciton absorption in thinner flakes[36]. Quereda et al.[37] showed that the optical absorption band edge could be tuned up to ~0.7 eV under both tensile and compressive stress. Raman spectroscopy is another optical method commonly used to probe and characterize 2D materials[38]. Based on theoretical considerations, there are 6 Raman active modes out of all possible 12 lattice vibrational modes. However, only three of these modes are active in the normal experiment geometry, where laser illumination is perpendicular to phosphorene plane[39]. In a monolayer, these three active modes, e.g., $A^1_g$, $B_{2g}$, and $A^2_g$, produce Raman peaks at 362.5, 439.3, and 467.6 $cm^{-1}$, respectively[25]. Raman spectroscopy is an effective method to measure physical and chemical properties of phosphorene such as number of layers, phonon frequency, strain, surface functionalization, strain, etc. For example, Raman peaks redshift when the layer number of phosphorene or the temperature of the material increases, with the $A^2_g$ mode being the most sensitive[40]. Moreover, the strain-induced variation of Raman spectra[41] and the dielectric function[42] estimated for two different directions reveals a significant optical anisotropy proving a strong directionality reliance of phosphorene. Thanks to the above effects, light phase retardance or polarization techniques could be applied to investigate the orientation and anisotropy of BP flakes[33].

The in-depth characterization of phosphorene, such as that needed to control the material's quality during fabrication or post-fabrication processing, to measure anisotropic interactions along specific directions or to probe phosphorene's sensitivity to various species or environments, can typically be achieved by the combination of several different methods, which only together can reveal, directly or indirectly, the status of a phosphorene sample and its condition. On the other hand, photoluminescence (PL) can play a prominent quantitative role in phosphorene studies among other techniques, as it is highly sensitive to even small changes in the band structure, anisotropy, and defects of phosphorene samples and is capable of producing fingerprint-like characteristic spectra, which reflects these changes (see schematic in Fig. 1). It needs to be noted however that the use of PL for identification of ML phosphorene is still unclear due to the high instabilities of such structures. Besides, the lack of a high-scale synthesis method that could reliably produce environmentally stable phosphorene samples is a major drawback influencing the

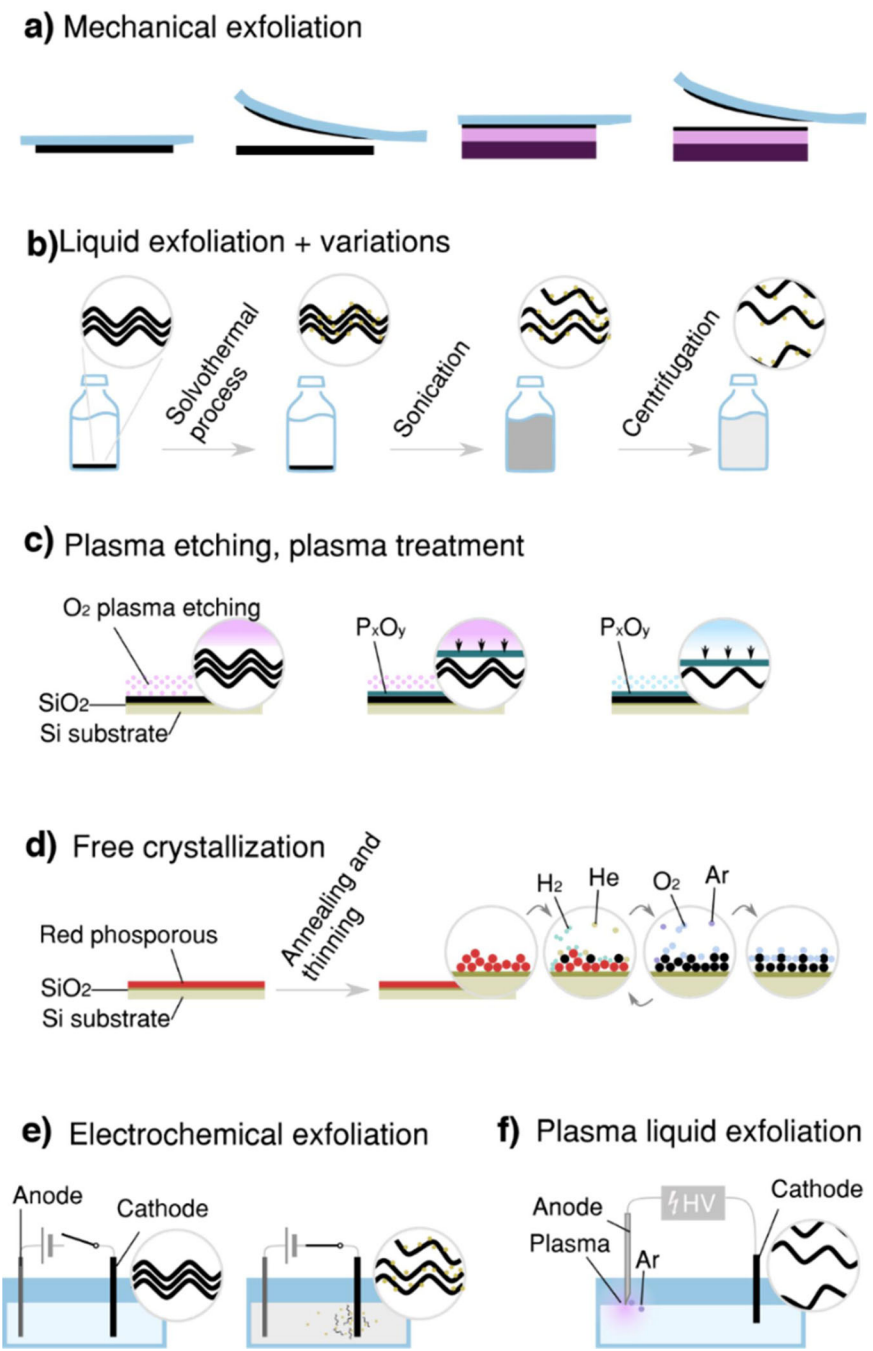


**Fig. 2 Fabrication methods. a–f** Various methods of single- and multilayer phosphorene flake fabrication.

limited number of PL studies allowing the in-depth fundamental understanding of the physics associated with radiative emission in this material (e.g., exciton dynamics).

Here, we provide a comprehensive review of PL as a versatile tool utilized efficiently in phosphorene studies presenting the current status, future challenges, and trends. We start with a short introduction to the properties, synthesis, and expansion of phosphorene in "Introduction." Then, we focus on the luminescence fingerprint of phosphorene and its excitation wavelength and thickness dependences in "PL and optical bandgap of BP." This section also reviews low-temperature studies of excitons and BP defects inducing PL tuning. In "Bandgap engineering in BP," we discuss bandgap engineering induced by geometric or structural modifications of BP, which could be probed by PL. We also deeply evaluated various environmental factors (e.g., strain, electric field) and chemical modifications of this surface affecting PL. Finally, we elaborate on the challenges and future perspectives in "Summary and outlook."

## PL AND OPTICAL BANDGAP OF BP

### The luminescence as a fingerprint of BP

PL is the spontaneous emission of light from a material under optical excitation[43]. This technique, similarly to some other optical spectroscopy methods, e.g., optical absorption, enables the investigation of the electronic band structures of materials with a nonzero optical bandgap, i.e., semiconductors[44]. In a typical PL experiment, a semiconductor is excited with a monochromatic

MOST WIEDZY Downloaded from mostwiedzy.pl

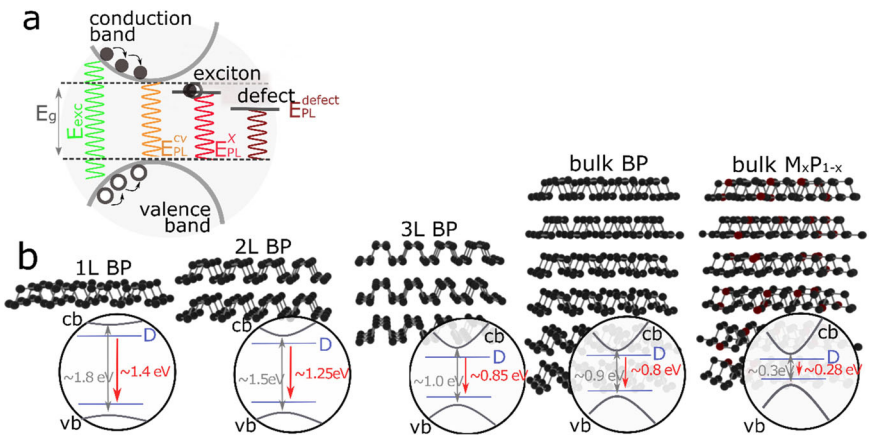


**Fig. 3 Bandgap of BP. a** Schematic illustration of excitation and emission processes in the vicinity of the bandgap occurring in an exemplary semiconducting material. $E_g$ is the energy of the electronic bandgap and $E_{exc}$ represents the excitation energy. $E_{PL}^{cv}$, $E_{PL}^{X}$, and $E_{PL}^{defect}$ denote the energies of different emissions due to the band-to-band (conduction-valence bands) transition, free excitons, and defects, respectively. **b** Schematic energy diagrams showing the electronic bandgap ($E_g$), and the exciton binding energy ($E_b$) dependent on the BP layers and metallic alloying.

light source (typically a laser with the emission between near-IR to UV) that provides photons of a given energy larger than the bandgap energy (Fig. 3a). The absorption of incoming photons leads to the excitation of electrons and a direct interband transition between the valence band (VB) and the conduction band (CB). Next, both types of charge carriers (i.e., electrons and holes) undergo energy and momentum relaxation due to scattering, such as Coulomb scattering or electron–phonon interactions, toward the local (in terms of k-vector) energy band minima. Finally, some of these carriers can recombine radiatively, which gives rise to the so-called band-to-band PL signal, as is depicted schematically in Fig. 3a. However, for this process to occur, both the energy and momentum conservation laws must be satisfied. Semiconductors are characterized by two basic types of bandgaps, i.e., direct and indirect. For the direct bandgap, both the CB minimum (CBM) and the VB maximum (VBM) are located at the same point of the Brillouin zone (BZ), e.g., Γ valley in GaAs, while the corresponding points are situated in different valleys of the BZ in the case of a material with an indirect bandgap, e.g., X and Γ points correspondingly for CBM and VBM in AlAs. Since the emitted photon can only carry out negligible momentum, the momentum conservation law can easily be fulfilled only for a direct bandgap radiative recombination. In this case, the carriers can recombine radiatively, while an additional mechanism involving scattering (e.g., phonons or crystallographic defects—disorder) is required for an indirect bandgap recombination. As a result, a direct bandgap PL is typically much stronger than an indirect one.

It is important to mention that the measured PL spectrum may not reflect the aforementioned band-to-band recombination processes of electrons and holes, but it may demonstrate emission associated with other processes. One of the most well-known process is the formation of a free exciton, i.e., electrostatically bound electron–hole (e–h) pairs. Due to their binding energy, the emission energy of excitons ($E_{PL}X$) is smaller as compared to that of the corresponding band-to-band transition ($E_{PL}^{cv}$). The detailed description of excitonic emission is discussed in "Low-temperature studies of excitons." Note that PL spectra of different materials may also be composed of other emissions which are at lower energies than excitons and are denoted as $E_{PL}^{defect}$ in Fig. 3a. Within this emission, we summarized all possible recombination processes giving rise to a PL signal, which can be divided into two groups. The first one is composed of nonexcitonic radiative recombination, which are a free electron with a neutral acceptor ($eA^0$), a free hole with a neutral donor ($D^0h$), and donor–acceptor pair transition with an electron from a neutral donor and a hole from a neutral acceptor recombine. The second group is formed by excitonic-like transitions, i.e., a free exciton bound to native defects, impurities (e.g., $D^0X$—an exciton bound to a neutral donor), and crystal imperfections, as well as so-called phonon replicas associated with the emission of phonons in addition to a photon. Note that the optical response of BP can also be modified due to the doping effects, e.g., both non- and intentional introduced in the growth of BP crystals or during postsynthesis processing. For example, doping can lead to the emission of charged excitons, which are three-particle complexes composed of an e–h pair and an excess carrier (an electron or a hole), see "Charged excitons" for details. Moreover, the optical properties BP are widely tunable and can be modified using various approaches, including layer thickness and doping control, as schematically depicted in Fig. 3b.

## PL of BP

The above-discussed possible recombination mechanisms, which are the sources of emission observed in PL spectra, depend strongly on the electronic properties of the material, its quality (e.g., impurities, defects, doping level, etc.), and, in particular, on the temperature at which the PL experiment is performed. Moreover, the shape and the intensity of the PL spectra can be significantly modified by changing the excitation energy in reference to the material's bandgap and absorption possible within its electronic structure. For example, the excitation in the vicinity of electronic or excitonic transitions provides so-called quasi-resonant conditions, which typically leads to the enhancement of the emission intensity. The other important aspect in selecting the excitation wavelength in a PL experiment is the penetration depth, which can be described by the Lambert–Beer law.

The PL is the prime nondestructive characterization tool for LMs, next to Raman scattering. Both techniques are commonly used to examine the number of layers in semiconducting LMs, such as transition metal dichalcogenides (TMDs), e.g., $MoS_2$, $WS_2$, and $MoTe_2$[45–49], and post-transition metal chalcogenides, e.g., InSe and GaSe[50,51]. In both cases, the PL spectra (energy and intensity) are modified substantially due to the indirect–direct bandgap transition during the decrease in the number of layers when going from a bulk material to a monolayer. BP also has a layer dependence of the energy of the optical bandgap energy from ~2.0 eV for the ML, through ~1.3 eV for the bilayer (BL), and down to 0.3 eV for the bulk state[52]. As the optical response of thin

MOST WIEDZY Downloaded from mostwiedzy.pl

layers of BP is dominated by the excitonic effects (discussed in detail in "Low-temperature studies of excitons"), the energy of the measured PL signal is related to the so-called optical bandgap, which is reduced in reference to the electronic bandgap (band-to-band transition) due to the binding energy of excitons. For a monolayer, the difference between the optical and electronic bands is extremely large at about 30% of the electronic bandgap and amounts to 940 meV[53]. A detailed description of the bandgap evolution as a function of the number of layers is presented in "From bulk to monolayer: layer-tuned PL." Note that the bandgap of BP remains direct for any thickness, and it is located in the Γ valley of the BZ. Moreover, the optical response of BP reveals a high in-plane anisotropic character, which allows optical determination of the crystalline orientation[54]. Figure 4 presents the thickness evolution of polarization-resolved PL spectra from ML to a tetralayer of BP. As mentioned above, the energy of the emitted light provides direct access to the information on the number of BP layers. At the same time, the in-plane angular dependence of the PL intensity reveals the crystallographic orientation of the BP crystal. As shown in Fig. 4, the emission is observed only for the x-polarization, which corresponds to the in-plane AC direction, while the signal intensity vanishes almost entirely for the y-polarization, which corresponds to the ZZ directions. This behavior originates from the crystal structure of BP. Particularly, the optical response of y-polarized light is strictly forbidden at the bandgap energy due to symmetry requirements. Thus, measuring the polarization properties of the PL signal can be used as a quick method to determine the crystallographic axis of thin layers of BP. This can also be employed for precise tuning of the twist angle between thin layers of BP, e.g., MLs, and to create artificial heterostructures known as twisted BLs or moiré superlattices, where quantum phases and strongly correlated phenomena emerge[55–57]. Recently, it has been demonstrated that the optical resonances in a phosphorene moiré superlattice formed by stacking of the ML and the BL depend significantly on the twist angle between the ML and the BL[58].

### The influence of the excitation energy on the PL

As discussed above, the PL signal depends on several factors, including the absorbance of the materials and the appearance of absorption processes. Figure 4g–k shows the optical absorption spectra of ML, BL, trilayer (TL), and bulk BP structures for incident light polarized along the AC and ZZ directions. As the excitonic effects determine the optical response of thin BP layers, one can focus on the red curves in Fig. 4g–k. It is seen that the absorption, and hence the penetration depth of the excitation light in PL experiment depends significantly on the number of phosphorene layers due to (1) the strong energy bandgap change, and (2) the evolution of the whole absorption spectra. Moreover, regardless of the layer's thickness, the light absorbance exhibits strong polarization effects due to the high in-plane anisotropic character of BP crystal. Consequently, the selection of excitation energy and polarization plays a crucial role for the PL experiment, as it determines its absorption efficiency and the shape of the measured emission spectrum.

### From bulk to monolayer: layer-tuned PL

As was mentioned, BP reveals a layer-dependent bandgap value. Consequently, PL characteristics can be used for the indirect estimation on the BP flake thickness adequately to the number of phosphorene layers. Figure 5 shows the normalized PL spectra of the mono (1L) to five (5L) layer BP samples[59]. The emission line measured for 1L phosphorene is at ~710 nm (~1.75 eV). This PL peak energy value was measured at ~10 °C (~263 K) and it is expected not to vary too much at room temperature (see ref. [59] for details). The measured emission lines for 2L–5L phosphorene at room temperature are observed at ~960 nm (~1.29 eV), ~1480 nm (0.97 eV), and ~1550 nm (~0.80 eV), respectively. It is important to mention that due to the direct nature of the bandgap in thin layers of BP, the corresponding PL intensities are bigger than those for silicon, which has an indirect bandgap[60]. Note that no protective layer has been used for the exfoliated monolayers, but they were kept in a chamber with a slow flow of protective nitrogen gas to prevent sample degradation during the experiments. PL spectra like those in Fig. 5a obtained for mechanically exfoliated BP have also been reported for thin layers fabricated through other methods[17]. One of the methods uses $O_2$ plasma etching[61]. Figure 5b displays the normalized PL spectra of thin-layer BP (from 1 to 4 layers) measured at room temperature, where the number of layers was finely tuned by etching in an $O_2$ plasma resulting in narrow and intensive PL peaks[61]. In order to prevent sample degradation, they used the thin surface layer of $P_xO_y$ which spontaneously formed in the plasma with an additional $Al_2O_3$ coating as protective environmental isolation. The emission lines for 1L–4L phosphorene are apparent at ~750 nm (1.65 eV), ~970 nm (1.28 eV), ~1290 nm (0.96 eV), and ~1440 nm (0.86 eV), respectively. The extracted energies are in very good agreement with the aforementioned results for mechanically exfoliated 2–4 layers[59], while there is a nonnegligible difference of about 40 nm (~100 meV) for a monolayer. It suggests that the effect of the surface modification (degradation) significantly affects the optical response for the monolayer BP, while it much less significantly influences the corresponding PL signal for thin layers with thickness >1L.

Figure 5c presents the layer dependence of the PL peak intensity of thin-layer BP. The significant decrease of the PL intensity of about 12.5 times is appreciated when the layer thickness is increased from 2L to 4L. Note that the intensity was normalized by layer number, which indirectly reflects the intrinsic luminescence quantum efficiency, $\eta_{PL}$. Furthermore, the electrical transition in phosphorene is characterized by the high radiative recombination rate, through which a strong photoluminescent response arises. The internal luminescence QE, which is indirectly represented as a normalized PL intensity, shows strong layer dependence. The luminescence QE depends on the rates of radiative recombination and electron relaxation, which are related to the band structure and layering of phosphorene[40]. Figure 5d summarizes the evolution of the reported PL peak energy (optical bandgap energy)[40,59,62–66] and the estimated energy of the electronic bandgap (band-to-band transition) with the phosphorene layer number. As can be appreciated from Fig. 5, the dispersion of the reported emission energies for monolayer BP is pronounced, i.e., the measured energies vary from ~1.3 eV to almost ~1.8 eV. It is a result of the largest influence of the surface (its oxidation, passivation, degradation, and other processes) on the optical properties of the monolayer BP. For the thicker BP layers, the energy dispersion is much smaller at about tens of meV, which suggests that the observed emission is mostly determined by the internal properties of the layers and the surface effects are negligible. Nevertheless, a significant monotonic decrease of the emission energies for thin-layer BP with increasing thickness from ~1.6 eV for a monolayer to ~0.8 eV for 5L is clearly observed. This demonstrates that the measurements of the room-temperature PL spectra of thin-layer BP can be used as an indirect method to estimate the layer thicknesses. To show the full picture, we also estimated the corresponding electronic bandgaps using the experimental data and the model presented in ref. [53]. Its observed dependence is analogous to PL energies, i.e., the substantial decrease when the thickness is increased. Moreover, it is seen that the obtained energy differences between the electronic bandgap and the PL emission, which correspond to the exciton binding energy (see the next section for details) also changes significantly as a function of the layer number. It reflects the different impact of the dielectric screening within the BP layer (strong screening) and

MOST WIEDZY Downloaded from mostwiedzy.pl

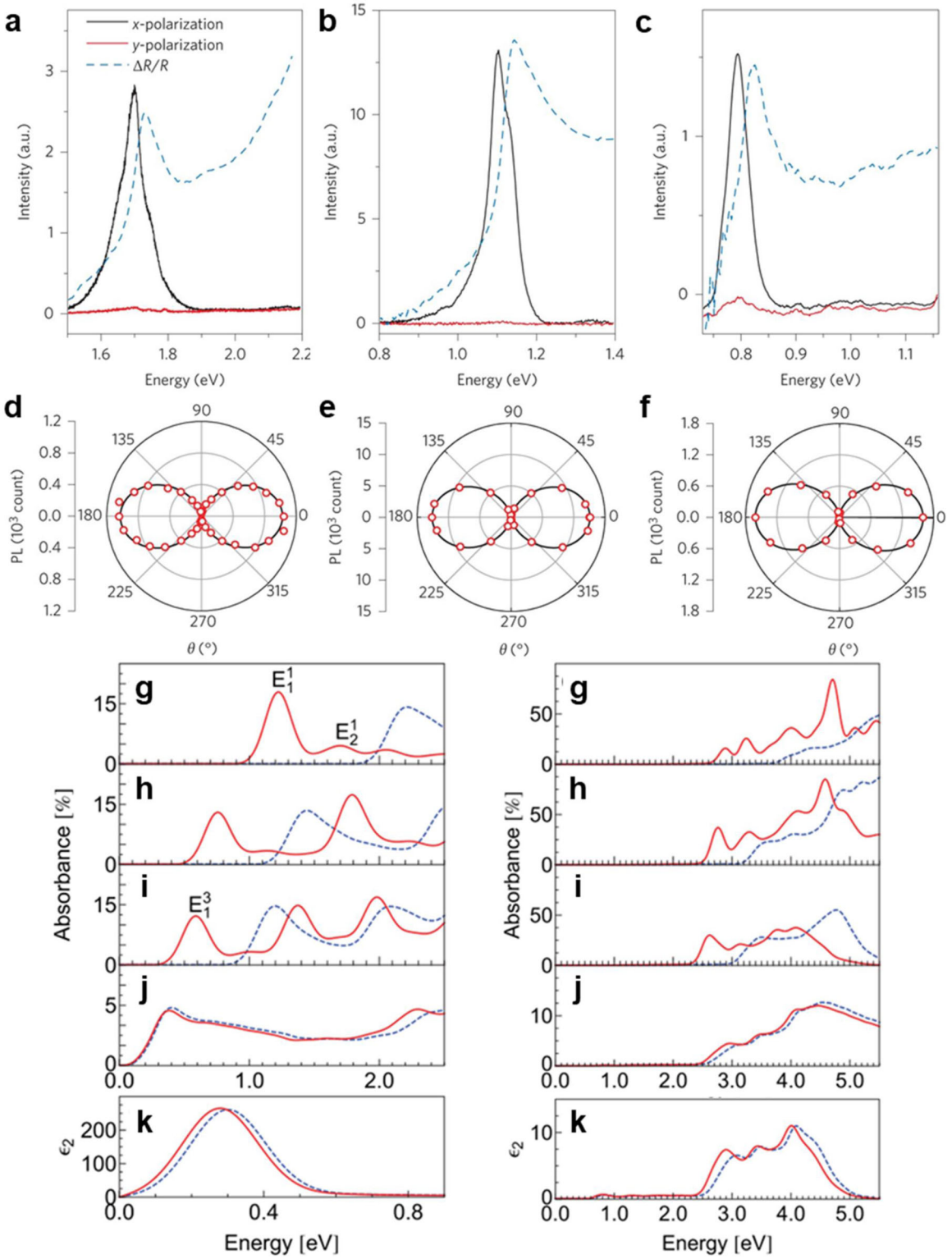


**Fig. 4 Polarization-resolved PL spectra of BP.** Photoluminescence of **a** monolayer, **b** bilayer, and **c** trilayer BP measured at 77 K with an unpolarized excitation of 2.33 eV. The blue dashed curves represent the absorption spectra. Intensity evolution of the PL at peak energy as a function of polarization angle θ. Data taken on **d** monolayer, **e** bilayer, and **f** trilayer BP are shown by the red circles. Black solid curves correspond to $\cos^2\theta$ dependence. The figure was reproduced with permission from ref. [164]. Optical absorption spectra of **g** monolayer, **h** bilayer, **i** trilayer, and **j**, **k** bulk BP for the incident light polarized along (left panel) the x (armchair) and (right panel) the y (zigzag) direction. In particular, **j** is the optical absorbance per layer in bulk BP. The single-particle optical absorption spectra are presented by dashed lines, while those spectra with e–h interaction included are presented by solid lines. The figure was adapted with permission from ref. [52].

MOST WIEDZY Downloaded from mostwiedzy.pl

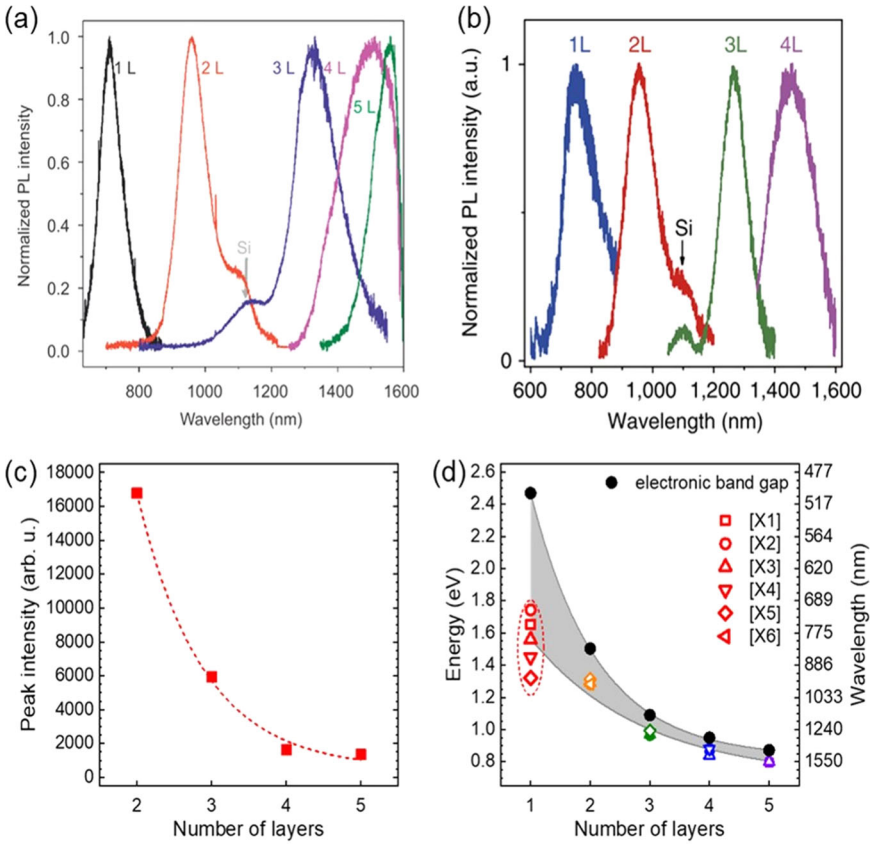


**Fig. 5 Layer number-dependent photoluminescence. a** Normalized PL spectra of the 1L–5L BP samples measured at −10 °C (1L) and at room temperature (2L–5L). Note that the thin layers were prepared using mechanical exfoliation. The figure was adapted with permission from ref. [59]. **b** Normalized room-temperature PL spectra of the 1L–4L samples fabricated by $O_2$ plasma etching. The figure was reproduced with permission from ref. [61]. **c** Layer dependence of PL peak intensity that is normalized by layer number. The dashed red curve is an eye guide. The figure was plotted using the experimental data presented in ref. [40]. **d** Evolution of (color open points) the PL peak energy (optical bandgap energy) and (black full points) the energy of the electronic bandgap (band-to-band transition) with the number of phosphorene layers. The shaded gray region is the eye guide corresponding to the exciton binding energy. The energies of PL peaks were taken from refs. [40,59,62–66], while the electronic bandgap was estimated using the experimental data and the model presented in ref. [53].

the surrounding media (weak screening) on the Coulomb interaction between an electron and a hole forming an exciton.

Similar layer-dependent PL characteristics have also been observed for thicker BP samples. The difference between the energy peaks for samples with thicknesses of 4.5 and 6 nm is still distinguishable. However, for thicker samples, e.g., with thicknesses of 30 and 46 nm, it is almost undetectable. Therefore, PL spectroscopy as a method for determining the number of layers in BP samples is effectively limited to few-layer phosphorene samples only[67]. In order to describe the origin of the observed PL evolution with the layer number of BP, we briefly analyze their crystallographic and electronic structure. Figure 6a presents the crystal structure of bulk BP, while the first BZ schemes of bulk and monolayer BP are shown in Fig. 6b. Bulk and monolayer BP have base-centered orthorhombic and simple orthorhombic crystal structures, respectively, both with four P atoms per primitive cell[68]. As can be seen in Fig. 6, there are two main in-plane directions, i.e., ZZ and AC, both in the monolayer and bulk forms. This implies that the corresponding BZ are also characterized by two inequivalent ZZ and AC directions, and leads to the anisotropic optical properties of BP discussed in the previous section.

Figure 6e shows the evolution of the calculated band structure with the number of layers, i.e., for 1L, 2L, 3L, and bulk. Two effects are apparent with the variation of the BP thickness: (1) a strong reduction of the electronic bandgap when the number of layers is increased and (2) insensitivity of the type and position of the bandgap—a direct one located at the Γ point of the BZ. However, it should be noted that the calculated electronic bandgaps are not consistent with the ones estimated in Fig. 5d. For monolayer, the theoretically calculated bandgap in Fig. 6e is underestimated versus the one in Fig. 5d (~2.1 eV versus ~2.5 eV, respectively), while the opposite situation takes place for 2L and 3L (~1.7/1.5 eV versus ~1.5/1.1 eV, respectively).

## Low-temperature studies of excitons

An exciton as a Coulomb-bound e–h pair is an elementary complex studied in semiconductors. Particularly, an optical response of the semiconducting TMDCs is dominated by the emergence of excitons[69,70] in which a bound e–h pair can move freely in the 2D crystal plane. Moreover, the binding energies of excitons are of the order of hundreds of meV and they can be tuned significantly by changing the number of layers and surrounding medium[69,71,72]. These excitons belong to the family of Wannier–Mott excitons, which are hydrogen-like systems of one positively and one negatively charged particle bound through electrostatic Coulomb interaction. Due to this similarity, the physics of excitons resembles that of hydrogen atoms. However, for the exciton, there is a screening of the Coulomb interaction due to the semiconductor's dielectric constant. In addition, in 2D materials, both bounded particles (i.e., electron and hole) are confined to the plane of the 2D material. Nevertheless, these excitons are characterized by a series of hydrogen-like excitonic states, so-called excitonic Rydberg series, labeled like in a

MOST WIEDZY Downloaded from mostwiedzy.pl

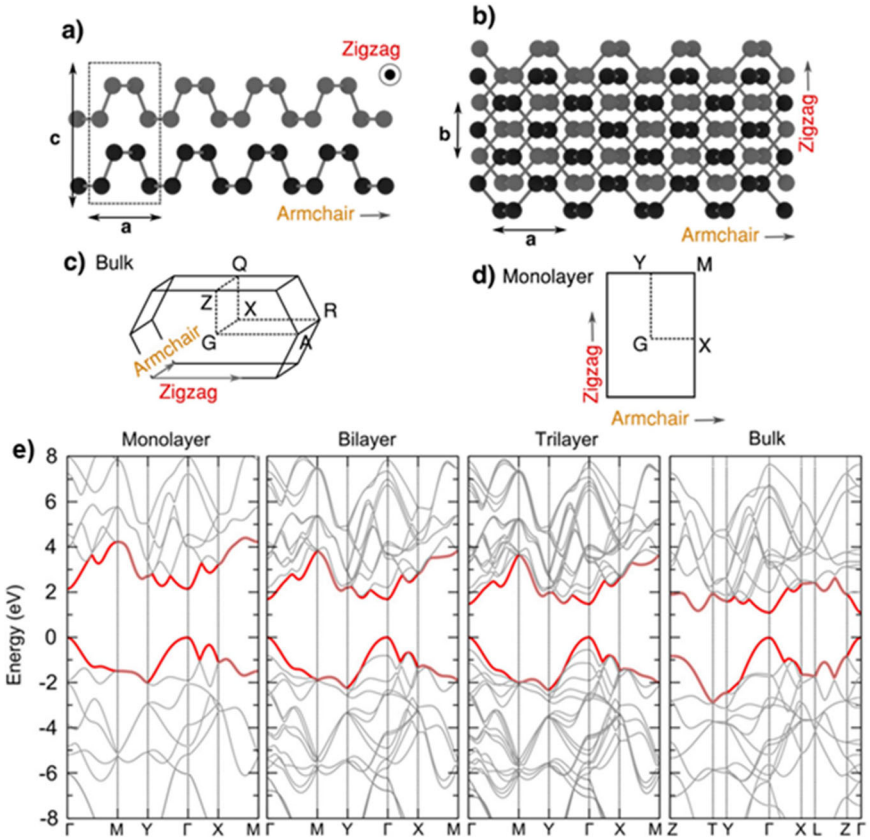


**Fig. 6 Band structure of layered phosphorene. a**, **b** Side (left) and top (right) views of the crystal structure of bulk black BP with respect to the in-plane zigzag and armchair directions. Monolayer BP corresponds to only the light or dark atoms. **c**, **d** First Brillouin zones of bulk (left) and monolayer (right) BP, where high-symmetry points are highlighted. **e** Calculated electronic band structure for monolayer, bilayer, trilayer, and bulk BP at all high-symmetry points in the Brillouin zone. The energy is scaled with respect to the Fermi energy. The figure was reproduced with permission from ref. [23].

hydrogen atom using main and angular quantum numbers, i.e., 1*s*, 2*s*, 2*p*, 3*s*, 3*p*, 3*d*, and so on, where 1*s* is a ground state and higher states are excited states. As the binding energies of these states decrease significantly with the increased main quantum number, the higher excitonic levels can be investigated only at sufficiently low temperatures[71,72]. In addition to neutral excitons, particularly at low temperatures, charged excitonic complexes with nonzero net charges can also be observed[73].

### A ladder of excitonic states

In order to study the sequence of excitonic states, not only the aforementioned low temperatures are required but specific experimental techniques also need to be applied. One of such methods to investigate a ladder of excitonic states is PL excitation (PLE) spectroscopy, which is a particular type of PL experiment. The PLE spectrum is obtained by monitoring of the intensity variation at specific emission energy under tuning of the excitation energy using a tunable laser. The first measured PLE spectrum on the BP ML reveals only the broad feature attributed to the excitation of the e–h pair directly to the electronic bandgap[74]. As it can be used for rough estimation of the binding energy of excitons, it is not sufficient to investigate the excitonic ladder. However, the recent progress in fabrication of high-quality samples opens this possibility[53]. Figure 7a shows the intensity of the PLE signal detected at the ground 1*s* state of the neutral exciton, i.e., the PL peak intensity of the 1*s* state as a function of excitation energy, together with the reflection contrast (RC) spectrum. RC spectroscopy is a type of absorption experiment in which one can probe mostly direct transitions in the system. The PLE of ML BP accurately reproduces all absorption resonances observed in the corresponding RC spectrum. Consequently, the observed features in both the PL and the differential reflection spectrum were assigned as excitonic series with the labels of 1*s*, 2*s*, 3*s*, and 3*d*. In order to study the excitonic ladder in ML BP, a theoretical analysis needs to be carried out. For BP, the description of excitonic states becomes more complicated due to the strong anisotropic properties. Figure 7b presents a schematic illustration of in-plane Coulomb screening of excitons in BP, which originates from the twofold rotational symmetry of thin layers of BP. At the same time, the wave function of the BL 1*s* state in real space is also characterized by strong in-plane anisotropy, as shown in Fig. 7c.

Figure 7d presents, extracted experimentally and calculated theoretically, the excitonic ladder for BL BP. Description of the excitonic ladder in thin flakes of LMs, such as BP, is not a straightforward task. Particularly, the dielectric inhomogeneity of the structures, e.g., MLs are surrounded by alien dielectrics may results in significant modification of the energy ladder of excitonic states and its deviation from the standard hydrogenic Rydberg series in two dimensions[75]. At large e–h distances (for higher states, e.g., 3*s*, 4*s*, and so on), the Coulomb interaction scales with the dielectric response of the surrounding medium, whereas it appears to be significantly weakened at short e–h distances (particularly for ground 1*s* state) by the usually stronger dielectric screening in the 2D plane. Consequently, the Rydberg series of *s*-type excitonic states in these 2D semiconductors does not follow the standard model of a 2D hydrogen atom[76], which characteristic energy ladder of states is described as $\sim 1/(n-1/2)^2$ with a principal quantum number *n*. The second particularly important

MOST WIEDZY Downloaded from mostwiedzy.pl

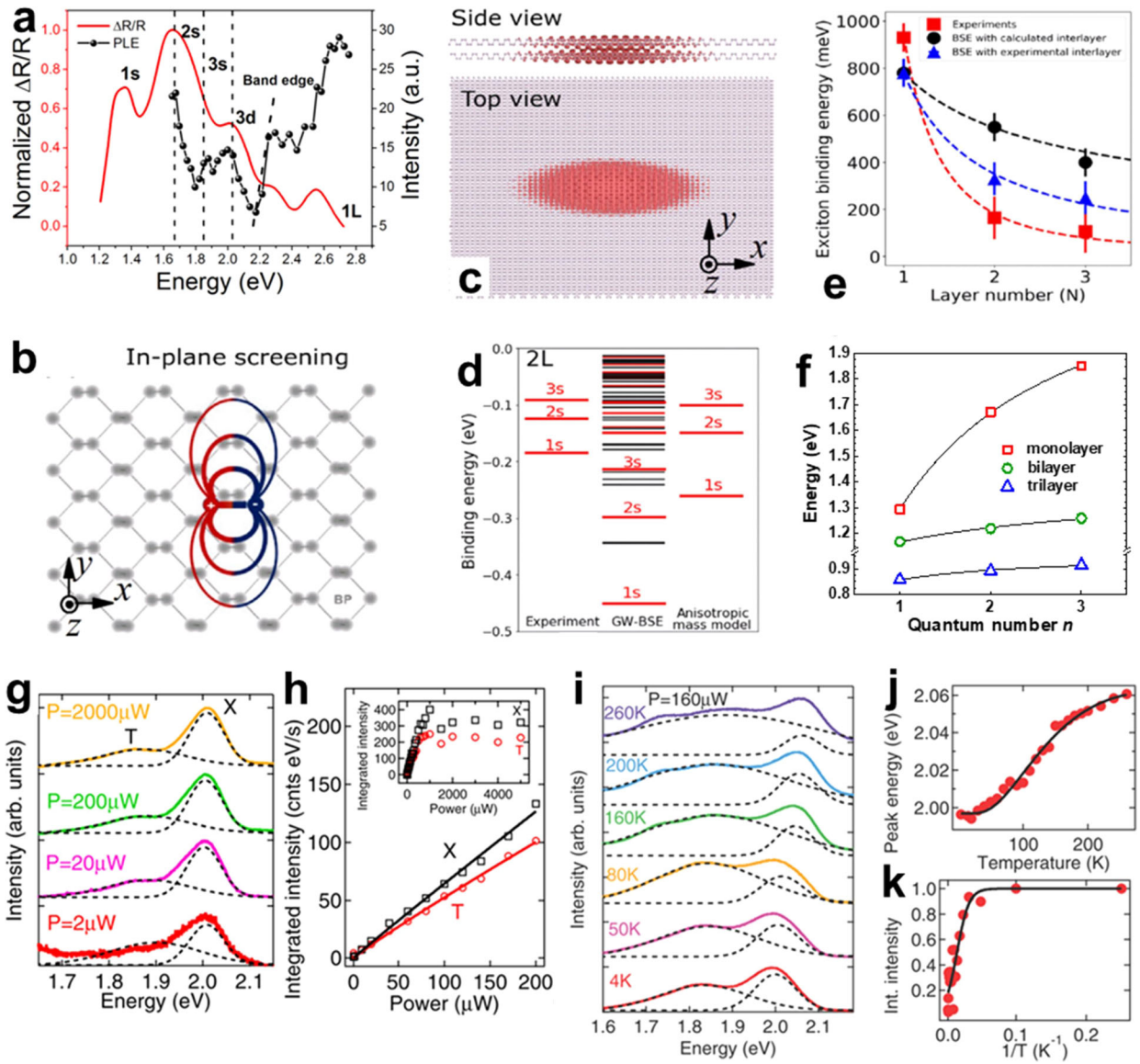


**Fig. 7 Excitons in BP. a** PLE intensity (right axis) at the emission peak of the monolayer BP as a function of excitation photon energies. The reflectance contrast spectra (left axis) are also superimposed for comparison. **b** Schematic of in-plane anisotropic Coulomb screening of excitonic states in BP. x, y, and z denote armchair, zigzag, and out-of-plane orientations, respectively. **c** Exciton wave function in real space of first bright state, i.e., the 1*s* state, for bilayer BP. The hole is fixed at the center. **d** Binding-energy spectrum of the excitonic series of the bilayer BP. Left panel: experimental results. Middle panel: GW + BSE calculation results. Right panel: calculation results of anisotropic effective-mass model. Bright states are in red and dark states are in black. **e** Exciton binding energy as a function of BP layer number, showing experimental measured binding energies, BSE-simulated binding energies with the calculated interlayer distance, and BSE-simulated binding energies with the experimentally extracted interlayer distance. Error bars are based on standard deviation errors. The figure was reproduced with permission from ref. [53]. **f** Experimental transition energies for the exciton states as a function of their index, *n*, measured monolayer, bilayer, and trilayer of BP. The black curves show fits to the data with the model described by Eq. 3. The experimental data was taken from ref. [53]. **g** Normalized PL spectra of the BP monolayer at different excitation powers. **h** Integrated intensity of the charged (T) and neutral (X) exciton emission versus excitation power. **i** Normalized PL spectra of the BP monolayer measured at different temperatures. **j** Emission energy of the neutral exciton as a function of the temperature. **k** Integrated intensity of the neutral exciton versus temperature. The dashed lines are Gaussian fits. The solid lines are fits to the models. The figure was reproduced with permission from ref. [136].

aspect in investigations of binding energies of excitons in LMs is the quality of samples. For monolayers of TMDs, it has been demonstrated that their encapsulation in hexagonal BN (hBN) flakes significantly increases their quality, which opens the possibility to observe experimentally excited excitonic states. Consequently, the estimation unquestionably the binding energy of excitons requires the high-quality samples allowing to observe the excited states of excitons as well as using the proper theoretical models considering the effect of surrounding environment. A common approach to account for the excitonic spectra of TMDC monolayers refers to the numerical solutions of the Schrödinger equation, in which the e–h attraction is approximated by the Rytova–Keldysh (RK) potential[71,77]. In the limit of an infinitely thin 2D slab (in our case, a monolayer) and reasonably large dielectric contrast between the 2D material and the surrounding materials, the RK potential, can be expressed analytically as[72,78]

$$V_{RK}(r) = -\frac{e^2}{8\varepsilon_0 r_0}\left[H_0\left(\frac{\kappa r}{r_0}\right) - Y_0\left(\frac{\kappa r}{r_0}\right)\right], \quad (1)$$

MOST WIEDZY Downloaded from mostwiedzy.pl

where $H_0$ and $Y_0$ are the Struve function and Bessel function of the second kind, respectively. The average dielectric constant of the encapsulating materials is given by $\kappa = (\varepsilon_{top} + \varepsilon_{bottom})/2$, where $\varepsilon_{top/bottom}$ is the dielectric constant of the surrounding medium. The dielectric properties of the 2D layer itself are characterized by its screening length $r_0 = 2\pi\chi_{2D}$, where $\chi_{2D}$, is the material's 2D polarizability. For anisotropic BP layers, the model needs to take into account that the reduced effective mass is anisotropic. This means that the anisotropic effective-mass model has been applied[79,80] and the exciton Hamiltonian reads

$$H = -\frac{\hbar^2}{2\mu_x}\frac{\partial^2}{\partial x^2} - \frac{\hbar^2}{2\mu_y}\frac{\partial^2}{\partial y^2} + V_{RK}(r), \quad (2)$$

where $\mu_x$ and $\mu_y$ are the reduced effective masses in the AC ($x$) and ZZ ($y$) directions, respectively. As is seen in Fig. 7d, the anisotropic mass model cannot describe the measured excitonic series. It is due to the effective-mass model being based on the isotropic dielectric constant, so it cannot capture the whole picture of exciton binding energy in the anisotropic BP. Moreover, the anisotropic mass in this model is characterized by an ellipse, while as shown in Fig. 7b, the effective mass is described by an approximate "8" shape. Thus, the results of the GW + BSE calculations do not illustrate the experimental results.

As the band-to-band transition was observed in ref. [53], the experimental exciton binding energies were extracted for ML, BL, and TL BP. It was found that the exciton binding energies decrease significantly from about 940 meV in a ML to about 160 meV in BL and around 110 meV in TL. These values determine that the excitonic effects dominate the PL spectra of thin BP layers even at room temperature. It is important to point out that the excitonic binding energy of a BP monolayer is a few times larger than the reported values for MLs of semiconducting TMDCs[71,73,81]. Like in TMDC monolayers[71,72,77,81], the surrounding dielectric environment can substantially modify the exciton binding energy. The observed energy separation between the 1$s$ and 2$s$ excitonic states of about 100 meV in a BP monolayer encapsulated in hBN flakes[82] is reduced three times compared to the case of a monolayer exfoliated on a modified $Si/SiO_2$ substrate (320 meV)[53]. Note that the 1$s$–2$s$ energy separation cannot be used to extract the exciton binding energy due to the dielectric inhomogeneity. As the theoretical models do not describe the exciton ladder to a sufficient level, the quasi-phenomenological approach proposed for semiconducting TMDC monolayers[71] can be very useful to determine the binding energies of excitons in thin layers of BP. It is proposed that the $s$-type Rydberg series of excitonic states follows a simple energy ladder

$$E_{ns} = E_g - R_y^*/(n+\delta)^2, \quad (3)$$

where $n = 1, 2, \ldots$ is the index of excitonic states and $\delta$ can be regards as adjustable parameters. $E_g$ represents the value of the electronic bandgap (band-to-band transition). $Ry^*$ is the effective Rydberg energy, scaled by the dielectric constant of the surrounding hBN medium and the reduced e–h mass, whereas the polarizability of the thin layer is accounted for only by $\delta$. Note that proposed formula coincides with the usual hydrogenic Rydberg series of energy levels of 2D and 3D excitonic states[76] with the $\delta$ parameter equal to 0 and 1/2, respectively. Surprisingly, it was demonstrated using this formula that $\delta$ is found to be close to zero for a $WSe_2$ monolayer encapsulated in hBN, whose exciton spectrum resembles that of a 3D hydrogen atom[71]. Moreover, the proposed formula coincides with that expected for a hypothetical hydrogen atom in fractional dimension $N$, ($N = 2\delta + 3$), which was indeed speculated to mimic the spectrum of Coulomb-bound states in low-dimensional semiconductor structures[83]. We used the discussed formula to describe the s-series of excitonic states in BP ML, BL, and TL reported in[53]. As only three excitonic states were observed, i.e., 1$s$, 2$s$, and 3$s$, to fit the proposed formula the values of electronic bandgaps were taken from the reflectance contrast data presented in the paper. Consequently, there are two fitting parameters: $Ry^*$ and $\delta$. As shown in Fig. 7f, the formula perfectly fits the data for thin-layer BP. The obtained binding energies of excitons ($E_b = R_y^*/(1+\delta)^2$) were found to be ~920, ~180, and ~90 meV for the ML, BL, and TL, respectively. The extracted values are in very good agreement with the corresponding aforementioned ones (940, 160, and 108 meV) obtained in ref. [53].

### Charged excitons

Charged excitons or trions are three-particle complexes composed of an e–h pair (exciton) and an excess carrier (electron or hole). Figure 7g demonstrates representative spectra measured at low, intermediate, and high excitation powers at the temperature of liquid helium ($T = 4.2$ K). The observed two emission lines are attributed to the neutral (X) and charged (T) excitons. The energy separation between the X and T lines defines the binding energy of a trion, which is found to be of about 120 meV and is in very good agreement with the reported value of ~100 meV measured at $T = 263$ K[59]. The extracted value is four times bigger compared to the reported values for MLs of semiconducting TMDCs[46,47,84]. Surprisingly, it was demonstrated recently that the encapsulation of the BP monolayer in thin layers of hBN leads to a significant reduction of the binding energy of a positive trion to about 30 meV[82]. This result indicates that the trion binding energy in BP monolayers can be modified using surrounding dielectric media. It is in contrast to the binding energies of charged excitons in TMDC monolayers, which stays at the same value regardless of the surrounding media[73].

The dependence of the integrated PL intensity of the X and T peaks as a function of the excitation power is shown in Fig. 7h. At low excitation powers (<1 mW), both intensities increase linearly with the power. At higher excitation powers (>1 mW), the T and X intensities saturate. This type of evolution is consistent with that reported in ref. [59] and confirms that the two observed transitions are related to the recombination of a single e–h pair. The temperature evolution of the PL spectra is shown in Fig. 7i. It is seen that the X emission blueshifts with increasing temperature, while at the same time the X line broadens. The behavior of the emission energy and the intensity of the excitonic peak is shown in Fig. 7j, k. The observed blueshift of the X line can be described in terms of the analogous temperature dependence of the bandgap of bulk BP. The anomalous temperature dependence of the bandgap of bulk BP arises from a combination of harmonic and lattice thermal expansion contributions, which are in fact highly intertwined[85]. With increasing temperature, the emission intensity of the exciton decreases, owing to the thermal activation of nonradiative recombination centers.

### Variation of BP PL induced by structural defects

The properties of 2D materials, especially those originating from the band structure, including light emission and PL characteristics, are dependent on intrinsic properties, such as chemical composition, crystal structure, number of layers, etc. However, they are also strongly dependent on structural defects and other forms of disorder, which can be categorized as intrinsic or extrinsic in nature. Like in the case of bulk (3D) crystalline materials, the intrinsic disorder originates from crystalline imperfections and different types of defects, such as vacancies, adatoms and substitutional dopants, line defects, grain boundaries, edges, etc., most of which can strongly affect the material's characteristics[86–89]. Because of its puckered structure, phosphorene can facilitate different types of point defects[20], including vacancies[90] and self-interstitials[91]. Their formation energy is significantly lower[92] than that of point defects in graphene[93]. By varying the concentration of defects, the properties and performance of 2D materials can be widely influenced. For example, heavy

MOST WIEDZY Downloaded from mostwiedzy.pl

substitutional doping, so-called alloying, can lead to the formation of solid-state solutions (alloys) with dramatically different properties than those of the host materials. Because of their significance, homovalent alloys between phosphorene and other group V elements are discussed separately in "Chemical approaches to modify PL of BP." In addition to intrinsic defects, there are also different types of extrinsic sources of disorder in 2D materials. This is largely due to the fact that, unlike bulk crystals, 2D materials are almost entirely composed of surfaces and are therefore highly sensitive to the environment. Consequently, their properties can be strongly affected by factors such as surface impurities/dopants and functionalization, modifications of interlayer gaps by means of high-pressure or intercalation, the use of substrates[94,95] and coating layers, or by combining 2D layers with other materials, for example, to form heterostructures.

Understanding the influence of defects and controlling their concentration is the basis of so-called defect engineering[96,97]. In principle, the type of defects and their concentration can be controlled during the synthesis or through the postsynthesis processing of a 2D material. Defects can be introduced by methods such as ion or electron irradiations[98], oxidation, surface functionalization, layer-substrate interaction, etc. In general, defects can either lead to undesired/parasitic effects or can be beneficial to the material's performance. In 2D materials and other low-dimensional structures, the effects of defects can be especially strong because of the strong localization of the electron wave function[99]. Among undesired defect-related effects is that they can scatter charge carriers and excitons and play the role of exciton quenchers facilitating nonradiative recombination[100]. For example, in phosphorene, the quenching of the quasi-1D excitons[52] originates mainly from the collisions with local quencher states, similarly to what has been reported for other 1D-like systems[101]. Defects can also facilitate or accelerate the degradation of 2D materials that are air sensitive[102]. This is what happens in phosphorene, where vacancies play a key role in the degradation mechanism that involves photo-assisted oxidation with oxygen dissolved in atmospheric water at the surface of phosphorene flakes[13,103,104].

However, defects can also be beneficial. For example, they can provide bandgap states and enable the trapping of charge carriers and excitons, and therefore, can be used to obtain emission at frequencies and enhanced PL intensity[61]. Defects can also provide effective ways for radiative recombination even in indirect bandgap materials. They can lead to the formation of 0D- or 1D-like states which can act as photoluminescent centers for the efficient radiative recombination of excitons, trions, and other excitations. However, while defects can, in principle, improve the optical properties of 2D materials, the variation of their local atomic structures can result in energy level fluctuations and broadening of PL spectra.

Several recent studies have focused on using defect engineering for the modification of PL in phosphorene. Kuriakose et al. investigated the influence of Ar and $O_2$ plasma treatment on the optoelectronic properties of multilayer phosphorene flakes[105]. They observed no noticeable PL signal after the Ar plasma treatment. However, the $O_2$ plasma treatment led to the appearance of a prominent PL peak between 650 and 760 nm, which was attributed to an oxygen-related acceptor state near the CB and the resulting distributed VB state, formed by the hybridization of the p-orbitals of O and P atoms[21,106]. In another study, Pei et al. used an oxygen plasma to etch thick phosphorene flakes and fabricate ML phosphorene with a controlled concentration of defects showing efficient room-temperature emission in the near-IR region[61]. Such samples, fabricated by overetching of phosphorene ML, showed a decrease of the 750 nm PL emission peak, attributed to the trion (charged exciton) in a pristine phosphorene ML[59] and the emergence of two strong PL peaks at 780 and 915 nm, respectively (Fig. 8a). Using power-dependent PL measurements and previous predictions based on numerical simulations[21], the authors attributed the 780 and 915 nm peaks to oxygen defect-related localization of excitons. The temperature dependence of these peaks did not follow the temperature dependence of a standard semiconductor bandgap, indicating that potential fluctuation and band tail states were responsible for the exciton localization, as observed in other semiconductor systems[107–109]. Interestingly, the study showed that, unlike in ML TMDs, localized excitons in a phosphorene ML could be observed even at room temperature, most likely due to the large trapping energy[21]. The same group also studied the emission of defect-localized excitons in phosphorene samples deposited on oxide substrates grown by plasma-enhanced chemical vapor deposition (PECVD)[64,110]. Their study of ML phosphorene samples showed two PL peaks at ≈700 and ≈920 nm, respectively[110]. The peak at ≈700 nm (labeled the A peak) (Fig. 8b) was attributed to the free excitons of the ML phosphorene in accordance with previous reports[59]. The peak at ≈920 nm (labeled the X peak in Fig. 8b) showed a considerably stronger PL intensity and was attributed to the excitons localized to interfacial local states[59]. The study also showed that these localized excitons exhibited linear polarization along the AM direction of the phosphorene lattice, similarly to what had been reported previously for the quasi-1D free excitons in pristine ML phosphorene. Beside this, the presence of these localized excitons at elevated temperature was also observed and the authors attributed it to the large trapping energy. Their similar study of three-layer (3L) phosphorene samples deposited on PECVD oxide substrates, showed a strong PL peak at ≈1430 nm from localized excitons, in addition to a free exciton emission at ≈1250 nm (Fig. 8d–h)[64]. Based on temperature PL measurements, they determined the activation energy of these localized excitons to have a large value of ≈77 meV, in agreement with the observed stability at higher temperatures (≈263 K).

## BANDGAP ENGINEERING IN BP

The emission of BP and its PL spectrum can be greatly modified using so-called bandgap engineering. While controlling the number of layers or using defect engineering are very important among such methods, there also several other bandgap engineering strategies that can be employed for tuning the PL of BP. This includes nanostructuring, the use of external fields such as strain or electric filed, and different chemical approaches, such as alloying, intercalation, and chemical surface modification.

### Nanoarchitectures and nanoribbons

As was shown, reducing the number of layers of BP, down to reaching the 2D regime, induces changes in the electronic structure and causes quantum confinement effects in one direction that result in the bandgap increase and modifications of DOS. Reducing the size of BP in other directions to form 2D, 1D, or 0D structures is an additional effective bandgap engineering approach. It also leads to other significant properties, including an enormous surface-to-volume ratio, large number of active sites, and many prominent edges, all of which are desirable for various technologies, including catalysis, electrochemical energy conversion and storage, photovoltaics, and sensing applications.

Phosphorene nanosheets (Fig. 9a) are MLs of BP, where phosphorus atoms are located at two atomic planes separated by a distance of ~1.90 Å. There are two types of bonds (in plane and out of plane) and two nonequivalent directions (AC and ZZ) in this structure. Consequently, phosphorene is a highly anisotropic material. It includes the band structure and optical properties. For example, phosphorene shows dichroism, i.e., polarization-dependent light absorption[111]. Phosphorene's mechanical properties are also highly anisotropic. Zhang et al. showed that when stress is applied, ML phosphorene is able to withstand a tensile

MOST WIEDZY Downloaded from mostwiedzy.pl

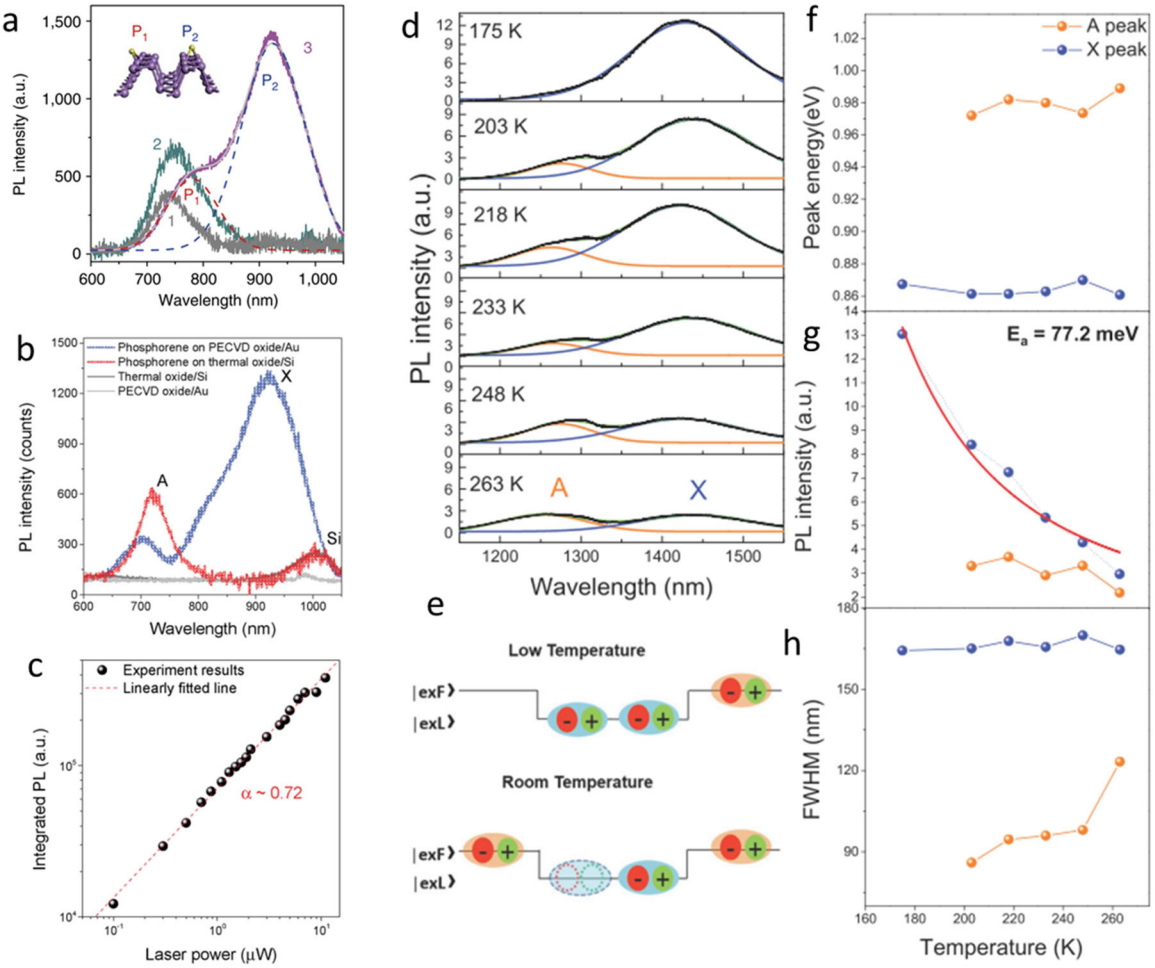


**Fig. 8 Photoluminescence from defect-bound excitons in phosphorene. a** Measured PL spectra of monolayer phosphorene samples produced by different methods: sample 1 exfoliated monolayer phosphorene (1), monolayer phosphorene with $P_xO_y$ capping layer fabricated by oxygen plasma etching (2), and monolayer phosphorene with $P_xO_y$ capping layer fabricated by oxygen plasma etching, but with overetching by oxygen plasma (3). The figure was reproduced with permission from ref. [61]. **b** Measured PL spectra of the monolayer phosphorene on PECVD oxide/Au (blue) and thermal oxide/Si (red) substrates. The measured PL spectra from the substrate background are also plotted for comparison. **c** Integrated PL of the low-energy X peak. The sublinear growth of integrated PL with the increased excitation power ($\alpha = 0.72$), indicating that the X peak at ≈920 nm is from localized excitons. The figure was reproduced with permission from ref. [110]. **d** Measured PL spectra at various temperatures for phosphorene 3L sample. **e** Schematic diagram showing the position of localized (low energy) and free (high energy) excitons at low temperature and elevated temperatures. Measured **f** peak position, **g** peak intensity, and **h** FWHM of PL peaks A and X as a function of temperature in 3L phosphorene. The figure was reproduced with permission from ref. [64].

stress up to 17.7 GPa in the ZZ direction and 7.6 GPa in the AC direction[112]. Figure 9g illustrates the band structure of a pristine BP nanosheet. The bandgap was calculated to be 0.869 eV, which is responsible for the semiconducting nature of a BP nanosheet. Moreover, the presence of a direct bandgap sets phosphorene apart from $MoS_2$ and $WS_2$, which display an indirect-to-direct bandgap transition when reduced to a monolayer[52,113].

Phosphorene nanoribbons are an example of a 1D phosphorus nanostructure, constructed from a single atomic layer in thickness and less than 100 nm in width. The key mechanical and electronic properties of nanoribbons depend mostly on their edge structures[114,115]. The ZZ nanoribbons (Fig. 9b) can be produced by separating a phosphorene ML perpendicular to the AC direction, by ultrasonicating in polar solvents, such as DMF or Nafion[27] following the red arrows in Fig. 9a. Except for the outermost edge atoms, ZZ nanoribbons undergo very little structural relaxation. They are however responsive to Peierls distortion, with unit-cell doubling[116]. The AC nanoribbons (Fig. 9c) are constructed by cutting a phosphorene ML parallel to the AC direction, as shown by the orange arrows in Fig. 9a. According to Guo et al., pristine ZZ nanoribbons exhibit a metallic character regardless of the nanoribbon width, whereas pristine AC nanoribbons are semiconducting in nature with an indirect bandgap (Fig. 9h), which decreases with increasing nanoribbon width[117]. However, doping AC nanoribbons with C, Si, and Ge can lead to the transition from semiconductor to metal[118]. The semiconducting character and relative width dependence of the bandgap of AC phosphorene nanoribbons are far more promising for possible application in FETs than graphene and $MoS_2$ nanoribbons, whose properties are strictly chirality dependent[119]. Moreover, high carrier mobility, small direct bandgap, and significant strain effects make AC phosphorene nanoribbons a promising material for nanoscale applications in FETs, IR photodetectors, and strain sensors.

Single-walled phosphorene nanotubes (SW-PNTs) can be constructed by rolling up a phosphorene monolayer. Two types of SW-PNTs are considered depending on the rolling direction, ZZ and AC (Fig. 9d, e). Theoretical studies have shown that for small diameters (12–19 Å) of SW-PNTs, the optimized unit-cell length in the axial direction is 3.30 Å and is independent on the diameter for AC PNTs,

MOST WIEDZY Downloaded from mostwiedzy.pl

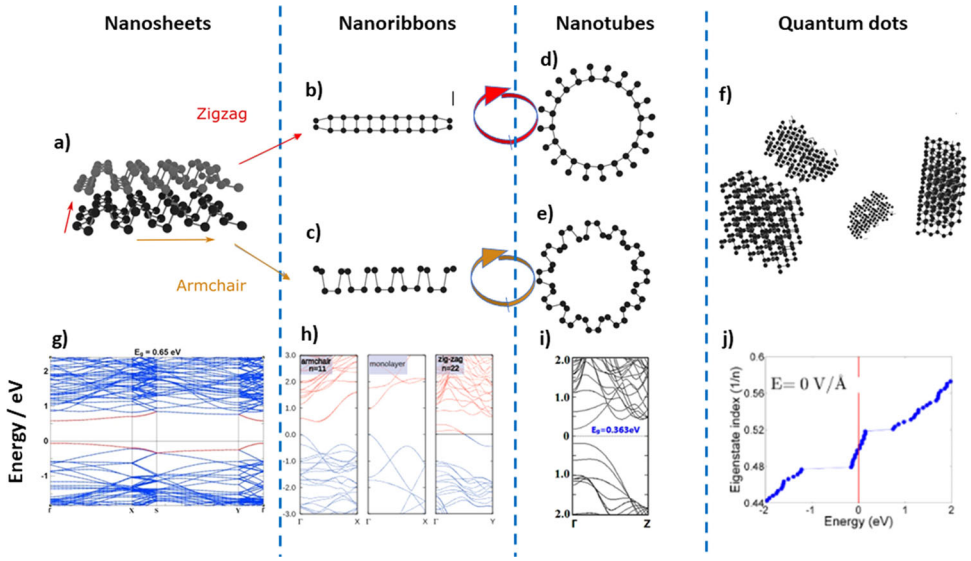


**Fig. 9 Phosphorene nanostructures.** Visual representation of **a** phosphorene nanosheet marked with armchair and zigzag directions; single phosphorene zigzag (**b**) and armchair (**c**) nanoribbon; **d**, **e** zigzag and armchair phosphorene nanotube, respectively, and **f** phosphorene quantum dots. The energy bandgap structure of **g** isolated phosphorene nanosheet. The figure was reproduced with permission from ref. [165]. **h** Phosphorene zigzag and armchair nanoribbons. The figure was reproduced with permission from ref. [116]. **i** phosphorene armchair nanotube. The figure was reproduced with permission from ref. [120]. **j** Energy levels of zigzag triangular phosphorene quantum dots. The figure was reproduced with permission from ref. [166].

whereas for ZZ PNTs, the optimized unit-cell length progressively increases from 4.13 to 4.48 Å for a diameter change from 12 to 17 Å[120]. For SW-PNTs, both AC and ZZ nanotubes are semiconductors (Fig. 9i), with the possible transition to a semimetallic behavior for ZZ nanotubes[117]. Yu et al.[120] showed that because of the huge difference in electron and hole mobility, AC phosphorene nanotubes can be considered as n-type semiconductors and can find applications in metal–oxide–semiconductor field effect transistors and optoelectronic devices. Allec et al.[121] calculated that PNTs exhibit a direct-to-indirect bandgap transition, with a decrease in the nanotube diameter. This transition is induced by competition in the energetic stability of various CB orbitals. Ansari et al.[122] showed theoretically that the mechanical properties of PNTs such as Young's modulus directly depend on the nanotube radius. Double-walled phosphorene nanotube (DW-PNTs) structures have also been studied computationally and have been shown to be more stable than the SW-PNTs. Moreover, Fernández-Escamilla et al.[123] claimed that DW-PNTs could be even more stable than a phosphorene monolayer. For the most stable DW-PNTs, the distance between the internal and external nanotube has been found to be similar to the distance between atomic layers in BP. Moreover, the bandgaps of DW-PNTs have been found to be smaller than the bandgaps of SW-PNTs of similar dimensions and they could be tuned by changing the diameter of either the internal or external nanotube.

Phosphorene quantum dots (PQDs), including nanodots and nanoparticles, are emerging functional 0D nanomaterials of dimensions usually around 3 nm in height and diameter (Fig. 9f). Ever since their first fabrication in 2015[124], PQDs have attracted a lot of attention because of their higher bandgaps, high surface-to-volume ratio, ultrasmall sizes, and more active edge sites per unit mass, as compared to 2D BP nanostructures. One of the most valuable properties of PQDs is the ability to control their bandgap via changing their diameter and as a result control their light absorbance and emission wavelength[125]. Moreover, PQDs exhibit a long exciton lifetime, modifiable surface and high PL quantum yield, which makes them promising for application in photocathodes, fluorescence probes, dye-sensitized solar cells, ion detection, and flexible memory devices[126]. Furthermore, due to their high biocompatibility and low phototoxicity, polymer-modified PQDs can be used in highly efficient cancer therapy, in vitro fluorescence, and in vivo thermal imaging. Gao et al. fabricated PQDs via small molecule-assisted liquid phase exfoliation with a nanoparticle size of 3.4 nm. UV–Vis–NIR absorption and Tauc analysis revealed that the bandgap of PQDs is equal to 1.81 eV (Fig. 9j), which is much higher than for other BP nanostructures of similar sizes[127].

## Effects of external fields

Strain engineering, i.e., the use of strain to modify the band structure and optical properties of BP, has been explored theoretically and experimentally. Seixas et al. used DFT calculations and consider the electronic and optical properties of phosphorene under uniaxial out-of-plane strain, in the regime comparable to what would be achieved using a diamond anvil cell[128]. They calculated that when the uniaxial strain is gradually increased from 0 to 5%, phosphorene undergoes a gradual transition from a direct to an indirect bandgap material. Moreover, the exciton binding energy reaches 0.87 eV at 5% of strain due to changes in effective masses. They also showed a linear strain dependence of PL and suggested using PL for the quantification of strain in phosphorene samples. San-Jose et al. used ab initio calculations to analyze the properties of excitons in strained FLBP and their dynamics under strain gradients[129]. They calculated an almost linear increase of the bandgap and exciton energy with uniaxial strain. For 5% of the strain, they found the increase of these energies to be about 0.4 and 0.6 eV for the ZZ and AC directions, respectively. They also found a strongly anisotropic inverse funnel effect, i.e., the efficient driving of excitons away from regions with high tensile strains (Fig. 10a).

Several experimental studies have also shown that 2D BP is highly sensitive to strain, and strain engineering of the bandgap and optical properties can be used effectively for this material. Using polarized IR spectroscopy, Zhang et al.[130] measured the bandgap increase by >20% with 1% uniaxial strain for a 6L BP (Fig. 10b, c). Interestingly, the effect had little dependence on the strain direction. This was also reported in a similar study by Zhang et al.[131] for a thicker 20 nm BP (Fig. 10d, e), where comparable bandgap strain coefficients of $99 \pm 4$ meV%$^{-1}$ in the AC direction

MOST WIEDZY Downloaded from mostwiedzy.pl

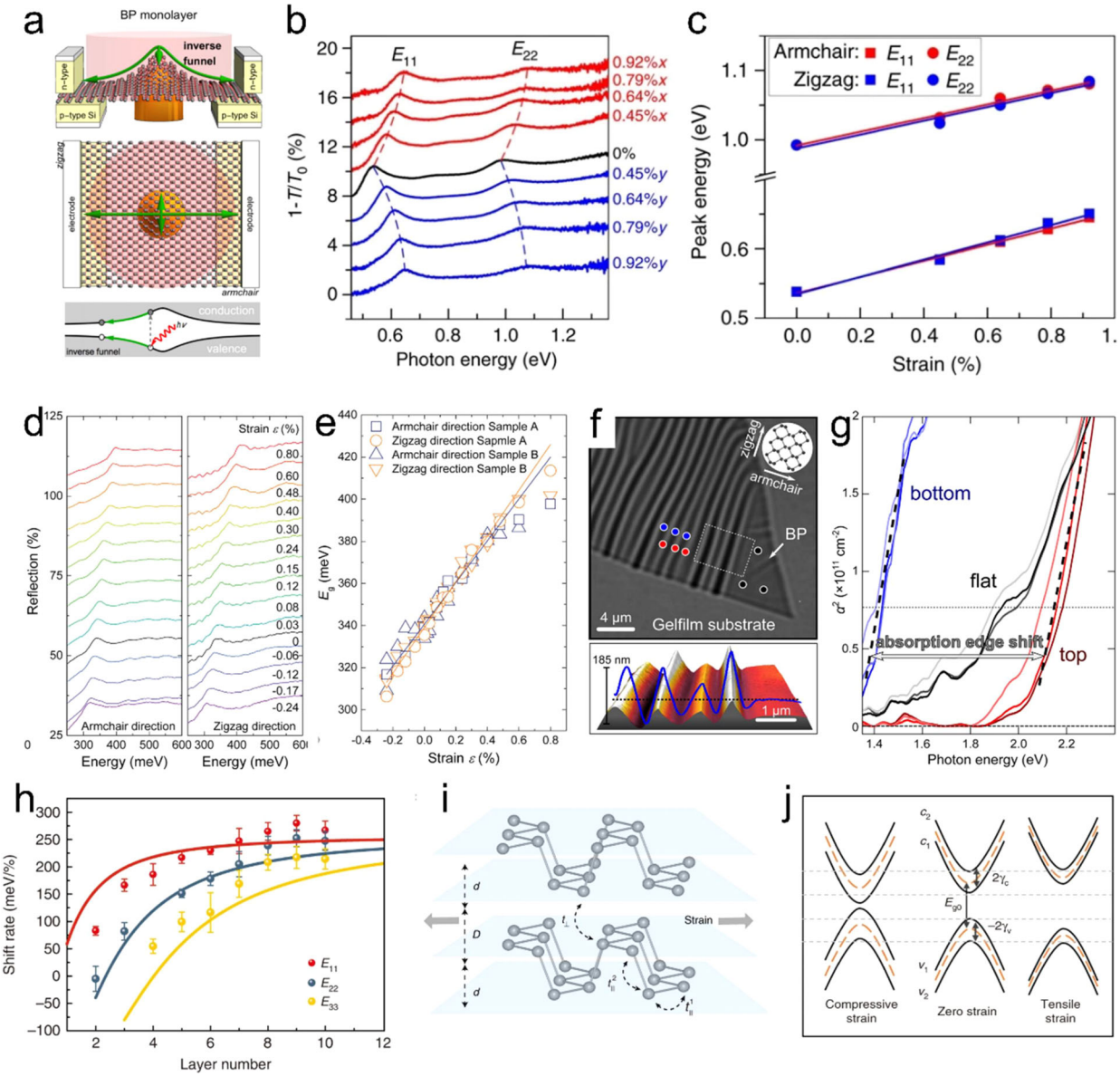


**Fig. 10 Strain engineering in BP. a** A highly anisotropic inverse funnel effect that pushes excitons away from the area of high tensile strain has been predicted in BP. The figure was reproduced with permission from ref. [129]. **b** Extinction spectra ($1-T/T_0$) of a 6L BP sample under varying tensile strains, with strain applied along the AC (red) and ZZ (blue) directions. **c** $E_{11}$ and $E_{22}$ peak energies as a function of tensile strains, the strain direction is along the AC (red) and ZZ (blue) directions, respectively. The figure was reproduced with permission from ref. [130]. **d** Evolution of absorption spectra with varying strains induced in AC (left) and ZZ (right) directions in 20 nm thick BP. **e** Bandgap plotted as a function of strain measured for two 20 nm thick BP samples. The figure was reproduced with permission from ref. [131]. **f** Transmission-mode optical image of ripples in a 10 nm thick BP flake. Below the optical image, an atomic force microscopy topography image acquired in the region highlighted with the dashed rectangle in **f** is shown. **g** Optical absorption spectra acquired on three ripple summits, three valleys, and three flat regions, indicated with colored circles in **f**. The figure was reproduced with permission from ref. [37]. **h** Averaged biaxial strain-induced shift rates of $E_{11}$, $E_{22}$, and $E_{33}$ peaks as a function of the layer number in 2–10L BP. **i** Illustration of 2L BP showing that when biaxial in-plane tensile stain is applied, the average distance between two layers ($D+d$) decreases due to the Poisson effect, while the gap between two layers ($D$) increases accompanied by a stronger decrease of the height of an individual layer $d$. **j** Schematic illustration of the band structure evolution of a bilayer BP under tensile and compressive strain. The orange dashed curves are the bands for a monolayer BP. The figure was reproduced with permission from ref. [132].

and $109 \pm 2$ meV%$^{-1}$ in the ZZ direction were obtained. Quereda et al. also showed strong strain-induced changes of the optical bandgap of BP, although in a much wider strain range[37]. They used transmission-mode optical microscopy of periodically strained BP samples (Fig. 10f) fabricated by the deposition of FLBP onto a prestretched elastomeric substrate with the subsequent release of the strain, and measured a large shift of the optical absorption band edge of up to ~0.7 eV between regions under a large tensile (+10%) and a large compressive (−30%) strain (Fig. 10g).

As shown by Huang et al., strain engineering can also be used to affect the optical response of 2D BP by modifying the interlayer vdW interactions[132]. By measuring the IR absorption spectroscopy of FLBP under in-plane biaxial strain and separating the interlayer

MOST WIEDZY Downloaded from mostwiedzy.pl

and intralayer contributions to the evolution of the band structure (Fig. 10j), they quantified the strain effect on the interlayer vdW coupling and showed that in-plane tensile strain can efficiently weaken this coupling. This surprising behavior originates from the puckered structure of BP. Although, the average distance between two adjacent layers decreases, when in-plane tensile stain is applied, the separation between two sublayers within each layer decreases even more (Fig. 10h, i).

2D layers of BP are often deposited on dielectric substrates. Moreover, because of stability concerns, they are also often covered by thin protective layers, such as graphene, h-BN, sapphire, etc. This, however, can affect the BP band structure and its optical bandgap. A recent DFT calculation[133] of the optical spectrum of 2D BP with a thickness of one to four layers, with and without encapsulation between h-BN and sapphire, showed the strong sensitivity of BP to environmental screening. As shown by this study, the encapsulation reduces the exciton BE in a monolayer by almost 70% and leads to the complete disappearance of a bound exciton in the four-layer BP structure.

The most common method to investigate the carrier concentration effect on the PL spectra in LMs is fabrication of back-gated structures[46,134,135]. This method, based on the field effect and electrostatic doping, has been widely used for tuning the physical properties of 2D materials.

It employs a metal–oxide–semiconductor (insulated-gate) field effect transistor structure, where modulation of a gate voltage Vg leads the field effect and modulation of the carrier concentration in the 2D material, used as one the electrodes. Using this approach, the Fermi level and the associated properties such as DOS, electronic and optical properties, etc. of 2D materials can be widely tuned. Because of the finite breakdown voltage of the typically used insulating layer (i.e., oxides or h-BN), the degree of electrostatic doping in typical structures is limited. However, the application of ionic liquids as gating materials allows this to be increased significantly, even by an order of magnitude, the achievable carrier doping densities, allowing for much stronger tunability of the physical properties of 2D materials. The field effect and electrostatic doping has been widely used to study various 2D materials. There are several reports of using this approach for 2D BP.

Figure 11a shows the PL spectra of the TL BP under various back-gate voltages at room temperature. The measured PL spectra exhibit two clear peaks with central wavelengths at ~1100 nm (~1.127 eV) and ~1300 nm (0.954 eV), which are attributed correspondingly to the emission of the neutral ($A^0$) and positively charged ($A^+$) excitons. As can be seen in the figure, these two emission lines are sensitive to the applied back-gate voltage. The intensities and energy dependences of the $A^0$ and $A^+$ lines as a function of the gate voltage are shown in Fig. 11b, c. At a voltage bias of −50 V, positive charges are pumped into the phosphorene and the PL spectrum is formed only by the $A^+$ lines (the PL emission from neutral excitons is almost absent). As the voltage is decreased gradually from −50 to 50 V, the PL emission from the neutral excitons became increasingly prominent, while that of the positive trions simultaneously became progressively weaker. At the same conditions, the gate evolution of the energies of the $A^0$ and $A^+$ lines and hence the $A^+$ binding energy stays at almost the same level. The extracted binding energy of the trion in TL BP is on the order of 160 meV, which is a larger value compared to the case of the ML (100–120 meV) reported in refs. [59,136].

Another method to modify the PL response of BP is application of an external vertical (out-of-plane) electric field to a sample. In contrast to the modification of the doping level described above, the electric field affects the electronic bands of the sample. As can be seen in Fig. 11d, the electric field significantly influences the PL spectra of the 20-layer BP. The PL spectra are composed of a single peak, whose wavelength decreases by almost a factor of 2 from about 3.7 μm (~330 meV) at 0 V to around 7.3 μm (~170 meV) at 40 V, which is accompanied with a significant reduction of the PL intensity of about 4 times. Knowing the parameter of the structure (see ref. [137]), the applied field can be used to calculate the displacement field. For example, from the data shown in Fig. 11d, it was found that 40 V corresponded to the displacement field of 0.48 V $nm^{-1}$. Figure 11e presents the evolutions of the extracted experimentally and calculated theoretical bandgap of the 20-layer BP as a function of the displacement field. Note that for 20 layers of BP, the emission energy corresponds to the calculated bandgap, which indicates that the aforementioned excitonic effects can probably be neglected in this case of a thick BP flake. The comparison between the band structure of the pristine BP and the BP under the displacement field of 0.48 V $nm^{-1}$ near the Γ point is shown in Fig. 11f. As can be seen in the figure, the displacement field changes the bandgap energy, but it does not substantially affect the band's shape. While the bandgap reduces, the overlap of the electron and hole wavefunctions decrease with the increasing electric field, which leads to the decreased oscillator strength and hence the lower PL intensity.

## Chemical approaches to modify PL of BP

Chemical approaches to materials engineering include alloying, chemical doping, and intercalation of chemical species.

Intercalation, a process of inserting foreign ions or molecules into the gaps between vdW-bonded layers of LMs, is a powerful tool for tuning material properties, including their electronic structure and optical response[138]. There are different ways through which intercalation can affect a LM. One way is through controlled electrical charge doping due to the effective charge transfer between the intercalant species (donor or acceptor type) and layers of the host material. The carrier concentration and Fermi level can be widely tuned using this approach. Another important effect is that intercalation can affect the separation and interactions between adjacent layers. In particular, by weakening and, in some cases, suppressing the interlayer interactions, intercalation can effectively transform a LM into a set of individual isolated layers, which profoundly changes the materials' properties, including their emission spectra. Such an effect has recently been demonstrated in BP during electrochemical intercalation with molecules of cetyltrimethylammonium bromide (CTAB)[139], as summarized in Fig. 12. In situ PL measurements during this process have shown the gradual evolution of the emission spectrum and change of the PL peak position from ≈1.38 to ≈1.75 and finally to ≈2.26 eV (Fig. 12b). This behavior has been explained through the intercalation staging mechanism, i.e., a process where the intercalant species first occupy every third, then every second, and finally each interlayer gap. Therefore, the observed PL spectra are roughly those of TLs, BLs, and monolayers. They are slightly modified because the insertion of CTAB layers causes the formation of superlattice structures and some modification of the electronic structures. A model of the monolayer phosphorene molecular superlattice (MPMS) and its calculated corresponding electronic structure are shown in Fig. 12h, i, respectively. Intercalation of BP using several other intercalant species has also been reported in the literature[140–142]. However, no systematic PL studies have been conducted for these systems yet.

In 2D materials, the electronic band structure and its features, such as bandgap, type (direct or indirect), effective mass, carrier mobility, etc., can be tuned by changing the number of layers[143] surface functionalization[144,145], strain[146], external electric field[147,148], etc. Alloying can also be used for the band structure engineering; here, the composition[149,150] plays the role of an additional parameter that can be used to adjust the band structure, in some cases significantly if a composition-dependent structural phase transition takes place. In particular, alloying can be used to tune the bandgap. For example, since the bandgap of

MOST WIEDZY Downloaded from mostwiedzy.pl

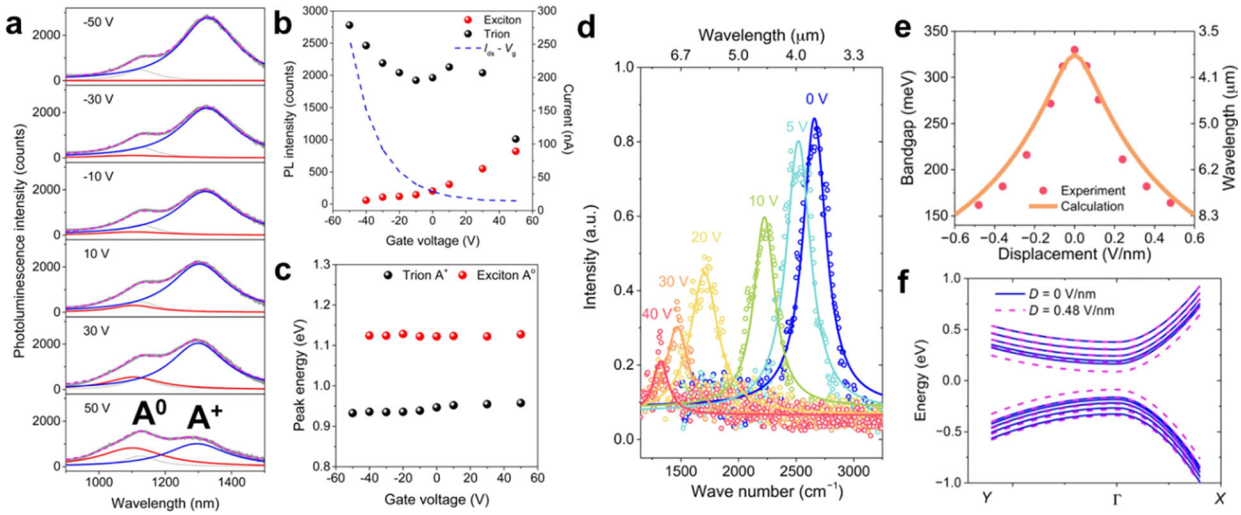


**Fig. 11 Photoluminescence as a function of carrier concentration. a** Measured PL spectra (solid dark gray lines) under various back-gate voltages. PL spectra are fit to Lorentzians. **b** PL intensity of exciton and trion (left), drain−source current as a function of gate voltages. The emergence of the charged exciton peak correlates with the onset of electrostatic doping. **c** Peak energy of exciton and trion as a function of gate voltage. The figure was reproduced with permission from ref. [63]. **d** Measured (dots) and fitted (lines) tunable PL spectra of the 20-layer BP device under different displacement fields from 0 to 0.48 V nm$^{-1}$. **e** Bandgap/wavelength tuning of the 20-layer BP extracted from PL spectra (dots) and first-principles based model calculations (line). **f** Bands of the 20-layer BP near the Γ point at the displacement field of 0.48 V nm$^{-1}$ in comparison with those of the intrinsic 20-layer BP. Only the five highest valence and five lowest conduction bands are plotted for simplicity of the models. The figure was reproduced with permission from ref. [137].

bulk BP is 0.3 eV and that of bulk arsenic is 0.15 eV, a continuum of intermediate values can be expected for the black phosphorous alloys in a wide range of compositions. However, there are limits for the alloy compositions within which the black phosphorous-like structure of the alloy is preserved. In general, elements of group V are known to form two types of layered structures, the so-called α (or A17) phase and β (or A7) phase[151]. The α phase has an orthorhombic honeycomb puckered crystal structure with the space group *Cmca*, while the β phase is a rhombohedral buckled layered crystal structure with the space group R3*m*. Although, both phases are layered, only the α phase is a vdW type of structure, while the β phase has the significant interaction of atomic orbitals between its layers. For phosphorus, the α phase, known as black phosphorous, is stable under normal conditions, while the β phase, known as blue phosphorene[152], is unstable. The situation is opposite in the case of arsenic (As), antimony (Sb), and bismuth (Bi). In this case, the β phase, known as gray As, gray Sb, and metallic Bi, respectively, is the most stable structure among the allotropes of these elements. Therefore, depending on the composition, *x*, the $M_xP_{1-x}$ (M = As, Sb, Bi) alloy compounds are expected to form the black phosphorous-like α phase, the blue phosphorus-like β phase, or segregate. Furthermore, the structural phase transition can be expected in these systems with the increasing composition (Fig. 13). This is supported by recent theoretical studies on the As–P alloys. Specifically, computational studies by Zhu et al. predict a phase transition from α-$As_{1-x}P_x$ to β-$As_{1-x}P_x$ when $x = 0.93$. The change in frontier states from electron lone pairs in α-P to σ bonds in β-As and the direct-to-indirect fundamental bandgap change is currently understood as the reasons for this phase change at critical composition[151]. An analogous approach considering only the total electronic energies revealed that the transition in $As_xP_{1-x}$ could occur at $x = 0.6$. But when also taking the thermodynamic energy terms into consideration, the critical As content shifted to a higher value of $x = 0.9$[153]. Interestingly, it has also been theoretically predicted that strain along the ZZ direction could trigger a semiconductor to metal phase transition in $As_xP_{1-x}$, whereas this transition does not seem to be possible along the AC direction[154]. In fact, the structural phase transition is expected to be accompanied by the electronic phase transition and possible direct-to-indirect bandgap transition. It is worth noticing that the critical composition where the phase transition occurs may depend on the number of layers. Due to their widely tunable electronic and optical properties, the $M_xP_{1-x}$ (V = As, Sb, Bi) alloys are promising candidates for application in the field of electronics and optoelectronics.

Covalent and noncovalent functionalization can be used to improve the environmental stability of 2D BP and help to enable its practical use in many technologies, such as the optoelectronics, electronics, and photonics fields. Interestingly, the interaction of BP layers with other compounds through covalent or noncovalent bonding affects their electronic structure, which affects the optoelectrical properties. Thereby, PL can be used to confirm such functionalization in an easy, fast, and nondistractive way. The choice of the solvent is very important for PL research. Firstly, an unsuitable solvent can cause erroneous measurements, such as in the case of N-methylpyrrolidone (NMP), which is the most popular solvent for BP liquid exfoliation. NMP degrades over time under ambient conditions and during sonication. Therefore, PL measurements of phosphorene produced by the liquid exfoliation method in NMP could be problematic[155]. Secondly, the PL spectrum of modified 2D BP is found to decrease and redshift with increasing polarity of solvent; the phenomenon that can be used to probe and study chemical modifications of BP samples. The effect of the solvent polarity, characterized by polarity index, $P'$ [156], is shown in Fig. 14a, where PL spectra from 2D BP samples dispersed in toluene ($P' = 2.4$), chloroform ($P' = 4.1$), and DMF ($P' = 6.4$) are compared. It can be seen that the PL spectra of these samples are gradually redshifted and broadened with increasing solvent polarity, which is directly related with the increase of the electron transfer between 2D BP and solvent molecules attached to its surface. Similar effects were also reported by Wang et al.[157] studying BP nanosheets functionalized with poly[(1,4-diethynyl-2,5-bis(hexyl-oxy)benzene)-alt-benzeno{c}thiadiazole] (PDBT) by using 4-bromobenzenediazonium tetrafluoroborate as a linker. Another example of using PL for the confirmation of BP

MOST WIEDZY Downloaded from mostwiedzy.pl

MOST WIEDZY Downloaded from mostwiedzy.pl





**Table 1.** Impact of solvent, excitation, and modification of phosphorene on shift of photoluminescence spectra emission peak.

| Starting material (SM) | Functionalized material (FM) | Solvent | Excitation [nm] | Peak of emission [nm] | | Description of functionalization | Ref. |
|---|---|---|---|---|---|---|---|
| | | | | SM | FM | | |
| BP nanosheets | PDBT-BP | Toluene | 502 | | 624 | BP nanosheets functionalized with poly[(1,4-diethynyl-2,5-bis(hexyl-oxy)benzene)-alt-benzeno{c}thiadiazole] (PDBT) by using 4-bromobenzenediazonium tetrafluoroborate (4-BBD) | 157 |
| | | Chloroform | | | 636 | | |
| | | DMF | | | 646 | | |
| Few layered BP nanosheets | Encapsulated BP nanosheets in micelles | | 300 | 353 | 352 | Helical copolymer based on polyethylene glycol and poly(phenyl isocyanide peptide) blocks is blended with a suspension of phosphorene nanosheets in order to be included in micelles | 159 |
| Polymer micelles | | | | 347, 405 | | | |
| Few layered BP | PDDF-g-BP | Toluene | – | – | 399 | Functionalization by using 4-bromobenzene-dizonium (4-BDD)-functionalized BP (4-BBD-BP) as a template for modified BP- poly[(1,4-diethynylbenzene)-alt-diphenylaminophenyl)fluorene] (PDDF) covalently grafted BP | 170 |
| | | THF | – | – | 402 | | |
| | | DMF | – | – | 413 | | |
| BPQDs | PFCz-g-BPGDs | Toluene | – | – | 397 | Functionalization of BPQDs under aqueous conditions by using a highly soluble diazotated polymer, PFCz-$N_2^+BF_4$. Poly[(9,9-dioctyl-9H-fluorene)-alt-(4-(9H-carbazol-9-yl) aniline)] (PFCz-NH2) was used as the synthetic precursor | 171 |
| | | THF | – | – | 403 | | |
| | | Chloroform | | – | 412 | | |
| | | DMF | | – | 421 | | |
| BPNPs | BPNPs@mSiO2 | - | 532 | 692.6 | 688.3 | A layer of mSiO2 was coated on the surface of the BPNPs via tetraethyl orthosilicate reaction | 172 |
| Phosphorene quantum dots | PQDs–tetracyanoquinodimethane (TCNQ) | Toluene | 360 | 413 | Redshift | Charge transfer interaction, donor and acceptor interactions | 162 |
| Phosphorene quantum dots | PQDs–tetrathiafulvalene (TTF) | Toluene | 360 | 413 | Redshift | | |
| Phosphorene quantum dots | PQDs–tetracyanoethylene (TCNE) | Toluene | 360 | 413 | Blueshift | | |
| BP nanoparticles | Cholesterol-modified black phosphorus nanospheres | – | 808 | – | 900–1650 | BP-cholesterol nanoparticles were encapsulated by DSPE-mPEG and L-a-lecithin | 173 |
| BP | Nile Blue-Black Phosphorus | Water | 570 | – | 680 | Nile blue diazonium tetrafluoroborate salt was synthesized to covalently modify BPs by aryl diazonium chemistry to produce stable and fluorescent NB@BPs | 174 |
| | | | 808 | | – | | |
| BPNPs | BPNPs-dabcyl-L | Tris-HCl | 200 | 524 | 525 | Fluorescence quenching was a consequence of the adsorption of dabcyl-Lprobe onto BPNPs | 160 |
| BP | BP-FKK | PBS | 450 | 562 | 525 | BP modified by tripeptide | 158 |
| | | | 325 | 380 | 415 | | |
| BPQDs | TbL3@BPQDs | NMP | UV illumination | – | 486, 540 583 | Ln (Tb, Eu, and Nd) coordinated BP structures exhibit fluorescence encompassing the visible to near-infrared regions | 175 |
| | EuL3@BPQDs | | UV illumination | – | 590<br>613<br>695 | | |
| | NdL3@BPQDs | | 730 | – | 903<br>1061 | | |
| Phosphorene | Phosphorene-$P_xO_y$ + 5 nm of ALD ($Al_2O_3$) | Flow of $N_2$ gas, −10 °C | 532 | 750<br>970<br>1290 1440 | 750<br>970<br>1290 1440 | Layer-by-layer thinning of BP by O2 plasma, followed by Al2O3 coating. PL for 1, 2, 3, and 4-layer BP, respectively | 61 |
| FLBP | FLBP–azidobenzoic acid | – | – | 1117[a] | 1442[a] | | 163 |

**Table 1** continued

| Starting material (SM) | Functionalized material (FM) | Solvent | Excitation [nm] | Peak of emission [nm] | | Description of functionalization | Ref. |
|---|---|---|---|---|---|---|---|
| | | | | SM | FM | | |
| BP flake | Fct-BP | – | – | 305[a] | 249[a] | Few-layer black phosphorus (FLBP) functionalized by 4-azidobenzoic acid<br>Modification of surface BP by immersion in 10 mM 2,2,6,6-tetramethylpiperidinyl-N-oxyl (TEMPO) and 10 mM [Ph3C]BF4 solution in a mixture water and acetone (1:1, v/v) | 176 |

[a]Parameters calculated from bandgap.

modification is shown in Fig. 14c. The peptide (FKK) used in this work for the modification of BP had much stronger emission than that of bare BP. Therefore, the observed broadening and quenching of the PL peak emission in modified BP (BP@FKK (300)), in comparison with the PL from the peptide only, was a clear indication of the successful modification[158].

In addition to confirming the functionalization, PL can also provide information on the resulting structure of the modified BP. For example, the quenching of the PL peak of the polymer helix confirms the enclosing of BP nanosheets inside the polymer micelles. The strong emission band of the encapsulated BP nanosheets and the lack of influence of the solvent polarity indicate closing of the BP nanosheets inside the polymer and the intermolecular electron transfer (Fig. 14b)[159]. PL of 2D BP can also be used as a detection probe for molecules adsorbed on the BP surface[160,161]. Pumera et al.[160] indirectly employed this approach to detected cDNA by using BPNPs as fluorophores. They observed PL quenching after the adsorption of dabcyl-Lprobe on the surface of BPNPs. However, after the addition of cDNA to the BPNPs-dabcyl-Lprobe, a higher PL intensity of the BPNPs was observed. This was explained as the formation of a ds-cDNA-dabcyl-Lprobe hybrid complex and weakening of the interaction between the BPNPs and the physically adsorbed dabcyl-L (Fig. 14d).

PL can also be employed, as for example reported by Rao et al.[162], to examine PQDs and the impact of organic molecules (donors, acceptors) on the optical properties of PQDs (Fig. 14e–h). Organic molecules such as tetracyanoethylene (TCNE), tetracyanoquinodimethane (TCNQ), and tetrathiafulvalene (TTF) interact with PQDs through charge transfer and effectively quench PL as their concentration is increased (Fig. 14h). In their study, Rao et al. concluded that the impact of TCNE and TCNQ on the PL of PQDs is more notable than that of TTF, which suggests that the acceptor binds more efficiently with PQDs. DFT calculations of the band structure for the adsorption of these three typical organic molecules (i.e., TCNQ, TCNE, and TTF) on the surface of ML and FLBP have shown considerable charge transfer and strong noncovalent interaction, which lead to bandgap reduction (Fig. 14i–l). Surface functionalization and molecular doping is an effective method for modulating the electronic and optical properties of phosphorene and, hence, for facilitating the wider use of this material[127].

The effective use of PL as a probe of phosphorene's surface modifications is based on the premise that the functionalization changes the structure and optical properties, especially the bandgap. An example where such a change is shown is covalent functionalization of FLBP using 4-azidobenzoic acid, which causes an increase of the bandgap from 0.86 eV (1442 nm) for bare FLBP to 1.11 eV (1117 nm) for FLBP–azidobenzoic acid with double-bound configuration[163].

Table 1 summarizes most of the known PL peaks for phosphorene and for products of its functionalization. These data obtained using different solvents and under different excitations show the variety of phosphorene modifications and the effectiveness of PL in characterizing phosphorene-based structures obtained by surface functionalization.

## SUMMARY AND OUTLOOK

In summary, we have provided an overview of PL spectroscopy as a convenient, nondestructive, and yet robust method to characterize BP, especially its 2D form, phosphorene. We have reviewed the existing literature reports on the use of PL to study BP and discussed how different, both intrinsic and extrinsic factors affect the band structure and optical response of BP. Even based on the limited number of studies reported so far, it is evident that PL is an insightful method that can provide a wider range of

MOST WIEDZY Downloaded from mostwiedzy.pl

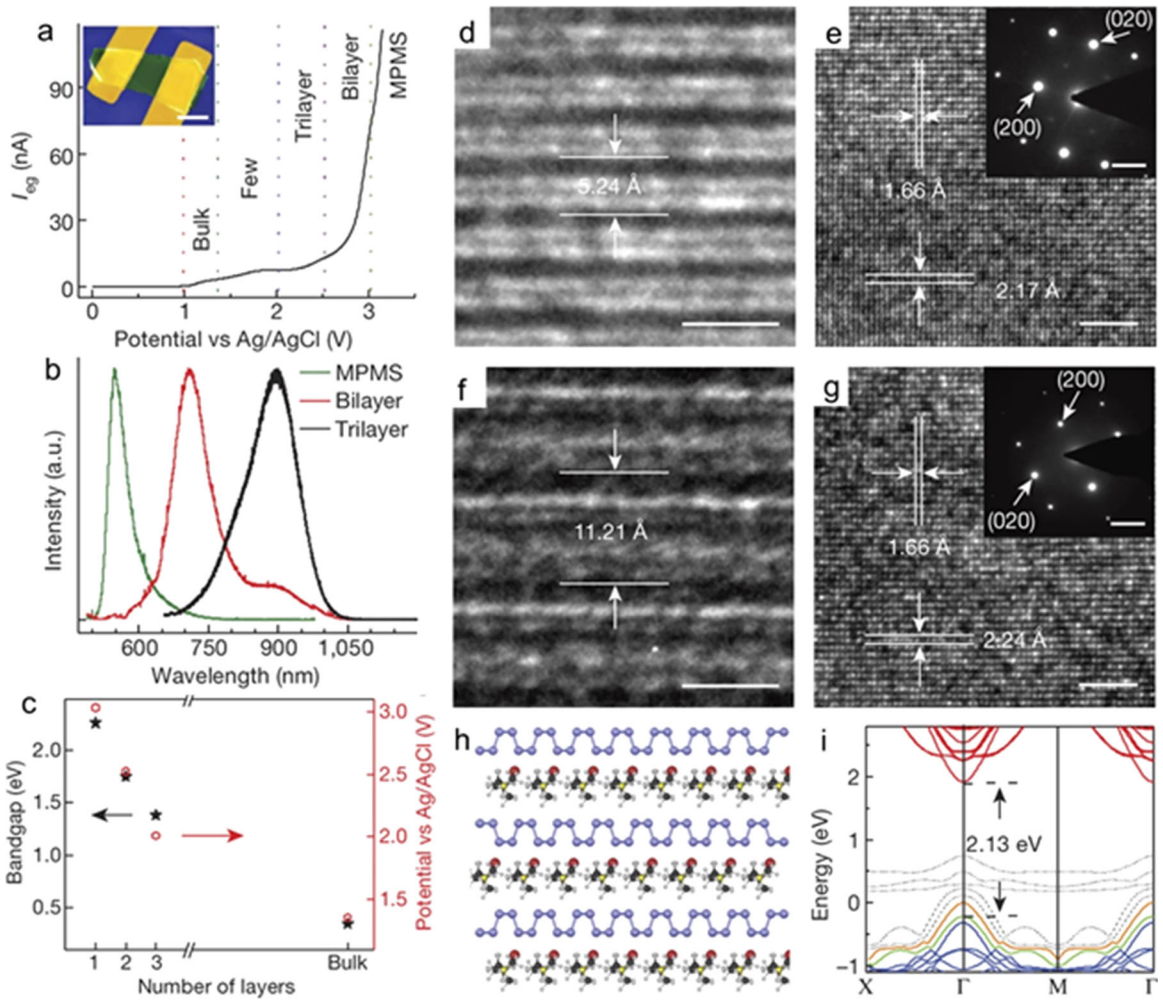


**Fig. 12 Effects of intercalation on the photoluminescence of BP. a** Electrochemical gate current as a function of the applied electrochemical potential (SEM image of the used transistor structure). **b** PL signals observed during different stages of intercalation. **c** Relationship between the bandgap or electrochemical potential and layer number, showing a good correlation between the electrochemical potential and the corresponding bandgap in the bulk, bilayer, trilayer, and monolayer regimes. High-resolution cross-sectional TEM image comparison between BP (**d**) and MPMS (**f**). Plane-view TEM images of BP (**e**) and MPMS (**g**) showing the lattice parameter expansion in the AC direction and negligible change in ZZ direction. Insets: electron diffraction of the corresponding TEM images. **h** Cross-sectional view of the simulated atomic structure of MPMS. **i** Simulated electronic structure of MPMS, demonstrating the enlarged bandgap of 2.13 eV in MPMS. The figure was reproduced with permission from ref. [139].

information. It can be used to characterize the quality of BP samples and to measure their intrinsic structural characteristics, such as number of layers, morphology, defects, etc. Similarly, it can also be used to probe external perturbations affecting the state of the sample, including temperature, strain, electric and other external fields, surface functionalization, effects of substrate/encapsulation proximity, etc. The advantages of using PL to characterize BP are that regardless of the number of layers, BP is a direct bandgap material that, in principle, can support efficient radiative recombination. Furthermore, due to the large exciton binding energy in thin layers, the corresponding efficient PL signal can be observed at high temperatures, even at room temperature. The challenges that still need to be addressed to fully utilize PL for detailed characterization of BP samples and for fundamental studies involving subtle effects inside the material will require high-quality samples. So far, most of the investigated BP samples exhibited significant inhomogeneities, which results in broadening of PL spectra, making this technique challenging for detailed, in-depth analysis. The development of synthesis methods of high-quality large-area BP will certainly help to advance this research. The other challenge is to suppress the degradation and control defects in BP samples. It is well understood that oxygen plays a key role in the degradation of BP and the degradation rate is layer dependent. Therefore, using PL for probing intrinsic properties of BP, especially in the case very thin samples, may require approaches that prevent exposure to oxygen. This may include: (1) using optical environmental cells, where the sample is held under inert atmosphere during PL measurement, (2) coating samples with optically transparent thin protective layers of materials such as h-BN and $Al_2O_3$, (3) measuring dispersions of BP in anhydrous organic solvents or deoxygenated water, and (4) functionalization of the BP surface to improve its stability. When such approaches are used, special care may however be needed during data collection and analysis. For example, interaction between BP and protective layer can modify the band structure of BP and affect its PL spectrum. Also, due to the puckered nature of a phosphorene layer, a uniform surface functionalization may not always be achievable leaving potentially uncovered regions prone to oxidation. Thus, the precise control of

MOST WIEDZY Downloaded from mostwiedzy.pl

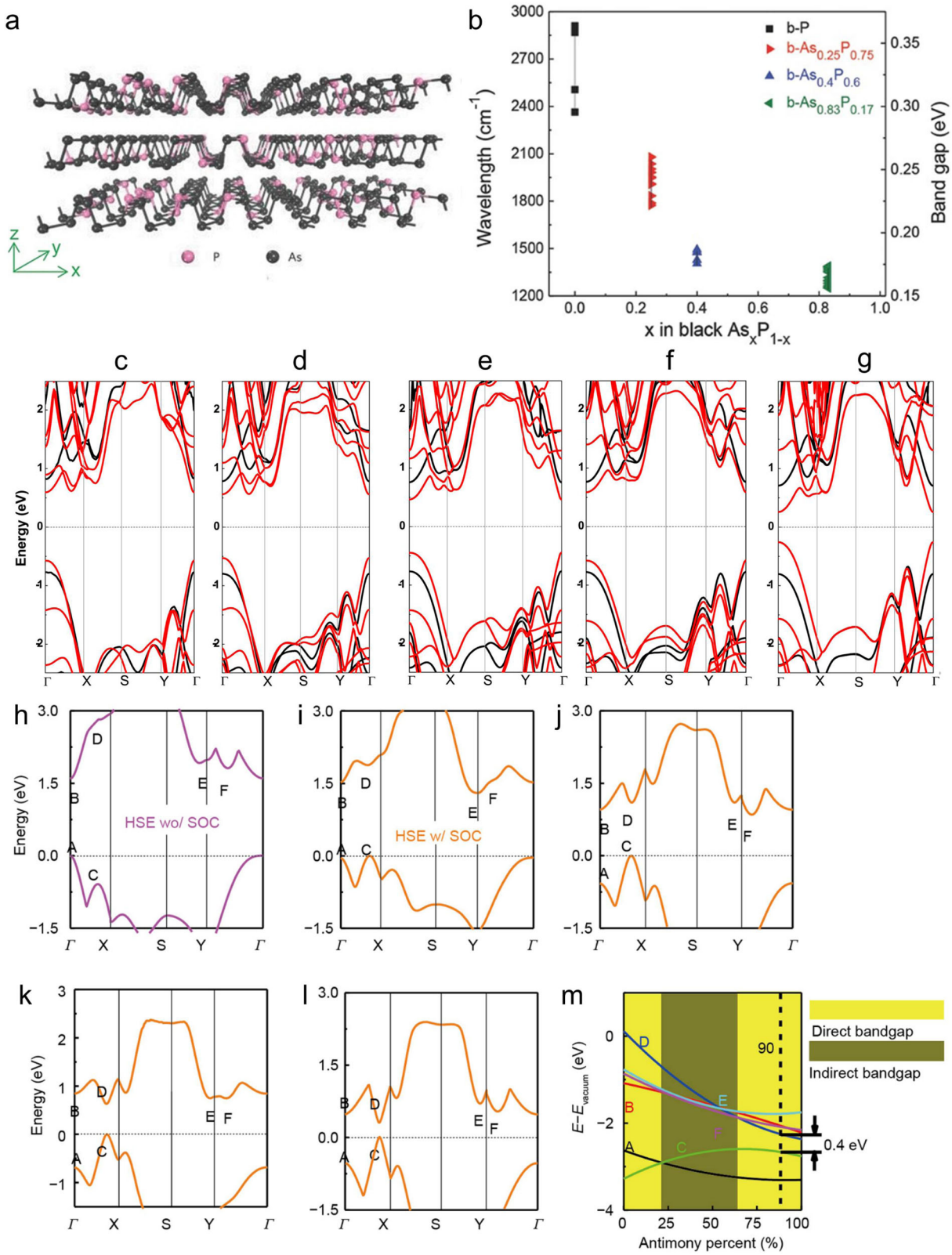


**Fig. 13 Bandgap engineering in BP-based alloys. a** Structure and exfoliation of layered b-AsP. **b** Summary of *x*-dependent bandgaps of b-$As_xP_{1-x}$. The thickness of the b-AsP flakes is >30 nm in these IR measurements. The figure was reproduced with permission from ref. [167]. Calculated band structures of $As_{1-x}P_x$ system: **c** pristine phosphorene ($x = 1$), **d** $As_{0.25}P_{0.75}$, **e** β-$As_{0.5}P_{0.5}$, **f** $As_{0.75}P_{0.25}$, **g** pristine arsenene ($x = 0$). The black line presents ML and the red lines BL. The figure was reproduced with permission from ref. [168]. VBM and CBM of **h** $Sb_0P_1$ (α-phosphorene), **i** $Sb_{0.25}P_{0.75}$, **j** $Sb_{0.5}P_{0.5}$, **k** $Sb_{0.75}P_{0.25}$, and **l** $Sb_1P_0$ (α-antimonene) monolayers, respectively. **m** Variation tendency of valence band state A, C, and conduction band states B and D–F. The yellow area represents that it is a direct bandgap semiconductor in this proportion range, and the dark yellow area is the indirect bandgap. The figure was reproduced with permission from ref. [169].

MOST WIEDZY Downloaded from mostwiedzy.pl

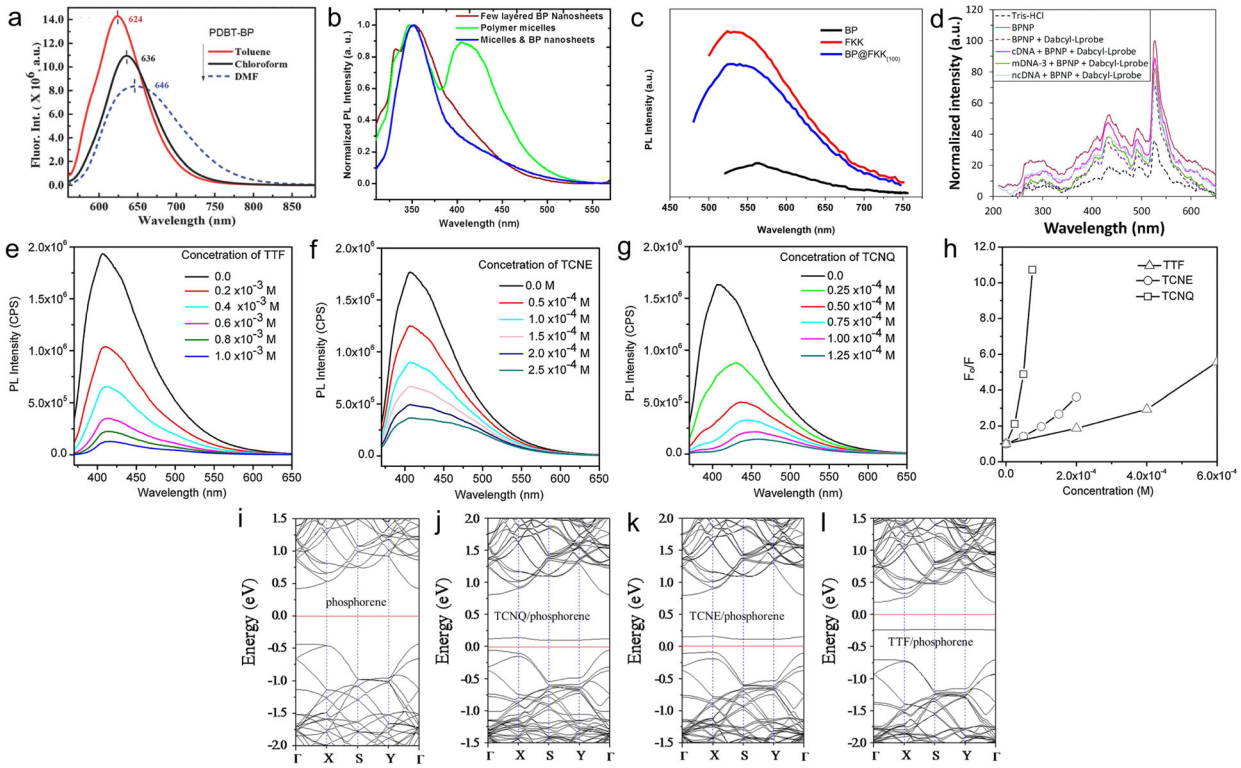


**Fig. 14 Impact of functionalization on the photoluminescence and band structure of phosphorene. a** Photoluminescence spectra of PDBT-BP in different organic solvents. The figure was reproduced with permission from ref. [157]. **b** Photoluminescence spectra of few layered BP nanosheets, polymer micelles, and encapsulated BP nanosheets in micelles. The figure was reproduced with permission from ref. [159]. **c** Photoluminescence emission spectrums of BP, FKK, and BP@FKK at the excitation of 450 nm. The figure was reproduced with permission from ref. [158]. **d** Fluorescence emission spectra of BPNP, Tris-HCl (buffer), dabcyl-Lprobe, BPNP with dabcyl-Lprobe (160 nM), and cDNA with dabcyl-Lprobe. The figure was reproduced with permission from ref. [160]. Quenching of photoluminescence of PQDs in toluene with different organic molecules: **e** TTF, **f** TCNE, **g** TCNQ, and **h** Stern–Volmer plots. The figure was reproduced with permission from ref. [162]. Band structures of **i** isolated phosphorene and phosphorene with: **j** TCNQ, **k** TCNE, and **l** TTF. The figure was reproduced with permission from ref. [127].

surface modifications and external perturbations is also critically important as PL is highly sensitive to these factors.

Received: 14 May 2021; Accepted: 9 September 2021;
Published online: 30 September 2021

## REFERENCES

1. Bagheri, S., Mansouri, N. & Aghaie, E. Phosphorene: a new competitor for graphene. *Int. J. Hydrog. Energy* **41**, 4085–4095 (2016).
2. Batmunkh, M., Bat-Erdene, M. & Shapter, J. G. Phosphorene and phosphorene-based materials—prospects for future applications. *Adv. Mater.* **28**, 8586–8617 (2016).
3. Eswaraiah, V., Zeng, Q., Long, Y. & Liu, Z. Black phosphorus nanosheets: synthesis, characterization and applications. *Small* **12**, 3480–3502 (2016).
4. Köpf, M. et al. Access and in situ growth of phosphorene-precursor black phosphorus. *J. Cryst. Growth* **405**, 6–10 (2014).
5. Wang, W., Zhang, Y. & Wang, Y.-B. Noncovalent π···π interaction between graphene and aromatic molecule: structure, energy, and nature. *J. Chem. Phys.* **140**, 094302 (2014).
6. Li, B. et al. Binding patterns and dynamics of double-stranded DNA on the phosphorene surface. *Nanoscale* **12**, 9430–9439 (2020).
7. Srivastava, A., Khan, M. S., Gupta, S. K. & Pandey, R. Unique electron transport in ultrathin black phosphorene: ab-initio study. *Appl. Surf. Sci.* **356**, 881–887 (2015).
8. Cai, Y., Ke, Q., Zhang, G. & Zhang, Y.-W. Energetics, charge transfer, and magnetism of small molecules physisorbed on phosphorene. *J. Phys. Chem. C* **119**, 3102–3110 (2015).
9. Abbas, A. N. et al. Black phosphorus gas sensors. *ACS Nano* **9**, 5618–5624 (2015).
10. Kim, J. et al. Observation of tunable band gap and anisotropic Dirac semimetal state in black phosphorus. *Science* **349**, 723–726 (2015).
11. Wang, G., Pandey, R. & Karna, S. P. Effects of extrinsic point defects in phosphorene: B, C, N, O, and F adatoms. *Appl. Phys. Lett.* **106**, 173104 (2015).
12. Huang, Y. et al. Interaction of black phosphorus with oxygen and water. *Chem. Mater.* **28**, 8330–8339 (2016).
13. Favron, A. et al. Photooxidation and quantum confinement effects in exfoliated black phosphorus. *Nat. Mater.* **14**, 826–832 (2015).
14. Wang, G., Slough, W. J., Pandey, R. & Karna, S. P. Degradation of phosphorene in air: understanding at atomic level. *2D Mater.* **3**, 025011 (2016).
15. Ahmed, T. et al. Degradation of black phosphorus is contingent on UV–blue light exposure. *Npj 2D Mater. Appl.* **1**, 1–7 (2017).
16. Kuntz, K. L. et al. Control of surface and edge oxidation on phosphorene. *ACS Appl. Mater. Interfaces* **9**, 9126–9135 (2017).
17. Kang, J. et al. Stable aqueous dispersions of optically and electronically active phosphorene. *Proc. Natl Acad. Sci. USA* **113**, 11688–11693 (2016).
18. Zhou, Q., Chen, Q., Tong, Y. & Wang, J. Light-induced ambient degradation of few-layer black phosphorus: mechanism and protection. *Angew. Chem. Int. Ed.* **55**, 11437–11441 (2016).
19. Island, J. O., Steele, G. A., van der Zant, H. S. J. & Castellanos-Gomez, A. Environmental instability of few-layer black phosphorus. *2D Mater.* **2**, 011002 (2015).
20. Hu, W. & Yang, J. Defects in phosphorene. *J. Phys. Chem. C* **119**, 20474–20480 (2015).
21. Ziletti, A., Carvalho, A., Campbell, D. K., Coker, D. F. & Castro Neto, A. H. Oxygen defects in phosphorene. *Phys. Rev. Lett.* **114**, 046801 (2015).
22. Kang, J. et al. Solvent exfoliation of electronic-grade, two-dimensional black phosphorus. *ACS Nano* **9**, 3596–3604 (2015).
23. Castellanos-Gomez, A. et al. Isolation and characterization of few-layer black phosphorus. *2D Mater.* **1**, 025001 (2014).
24. Brent, J. R. et al. Production of few-layer phosphorene by liquid exfoliation of black phosphorus. *Chem. Commun.* **50**, 13338–13341 (2014).
25. Guo, Z. et al. From black phosphorus to phosphorene: basic solvent exfoliation, evolution of Raman scattering, and applications to ultrafast photonics. *Adv. Funct. Mater.* **25**, 6996–7002 (2015).

MOST WIEDZY Downloaded from mostwiedzy.pl

26. Yasaei, P. et al. High-quality black phosphorus atomic layers by liquid-phase exfoliation. *Adv. Mater.* **27**, 1887–1892 (2015).
27. Kumar, A. Controlled nanostructures and simultaneous passivation of black phosphorus (phosphorene) with Nafion. *J. Mater. Res.* **35**, 141–152 (2020).
28. Lu, W. et al. Plasma-assisted fabrication of monolayer phosphorene and its Raman characterization. *Nano Res.* **7**, 853–859 (2014).
29. Rajabali, M. et al. High-performance phosphorene-based transistors using a novel exfoliation-free direct crystallization on silicon substrates. *Adv. Mater. Interfaces* **7**, 2000774 (2020).
30. Erande, M. B., Suryawanshi, S. R., More, M. A. & Late, D. J. Electrochemically exfoliated black phosphorus nanosheets—prospective field emitters. *Eur. J. Inorg. Chem.* **2015**, 3102–3107 (2015).
31. Huang, H. et al. Rapid and scalable production of high-quality phosphorene by plasma–liquid technology. *Chem. Commun.* **56**, 221–224 (2020).
32. Wang, X. & Lan, S. Optical properties of black phosphorus. *Adv. Opt. Photonics* **8**, 618–655 (2016).
33. Lan, S., Rodrigues, S., Kang, L. & Cai, W. Visualizing optical phase anisotropy in black phosphorus. *ACS Photonics* **3**, 1176–1181 (2016).
34. Chen, X., Sophia Ponraj, J., Fan, D. & Zhang, H. An overview of the optical properties and applications of black phosphorus. *Nanoscale* **12**, 3513–3534 (2020).
35. Sotor, J. et al. Ultrafast thulium-doped fiber laser mode locked with black phosphorus. *Opt. Lett.* **40**, 3885–3888 (2015).
36. Zhang, G. et al. The optical conductivity of few-layer black phosphorus by infrared spectroscopy. *Nat. Commun.* **11**, 1847 (2020).
37. Quereda, J. et al. Strong modulation of optical properties in black phosphorus through strain-engineered rippling. *Nano Lett.* **16**, 2931–2937 (2016).
38. Cong, X., Liu, X.-L., Lin, M.-L. & Tan, P.-H. Application of Raman spectroscopy to probe fundamental properties of two-dimensional materials. *Npj 2D Mater. Appl.* **4**, 1–12 (2020).
39. Ribeiro-Soares, J., Almeida, R. M., Cançado, L. G., Dresselhaus, M. S. & Jorio, A. Group theory for structural analysis and lattice vibrations in phosphorene systems. *Phys. Rev. B* **91**, 205421 (2015).
40. Zhang, S. et al. Extraordinary photoluminescence and strong temperature/angle-dependent Raman responses in few-layer phosphorene. *ACS Nano* **8**, 9590–9596 (2014).
41. Pyrchla, K. & Bogdanowicz, R. Density functional LCAO calculations of vibrational modes and phonon density of states in the strained single-layer phosphorene. *Appl. Surf. Sci.* **528**, 147033 (2020).
42. Xie, Z. et al. Electronic and optical properties of monolayer black phosphorus induced by bi-axial strain. *Comput. Mater. Sci.* **144**, 304–314 (2018).
43. Pelant, I. & Valenta, J. *Luminescence Spectroscopy of Semiconductors* (OUP, 2012).
44. Cardona, M. *Fundamentals of Semiconductors (Graduate Texts in Physics)* (ed. Cardona, M.) (Springer, 2010).
45. Lezama, I. G. et al. Surface transport and band gap structure of exfoliated 2H-$MoTe_2$ crystals. *2D Mater.* **1**, 021002 (2014).
46. Molas, M. R. et al. The optical response of monolayer, few-layer and bulk tungsten disulfide. *Nanoscale* **9**, 13128–13141 (2017).
47. Arora, A., Nogajewski, K., Molas, M., Koperski, M. & Potemski, M. Exciton band structure in layered MoSe 2: from a monolayer to the bulk limit. *Nanoscale* **7**, 20769–20775 (2015).
48. Arora, A. et al. Excitonic resonances in thin films of WSe 2: from monolayer to bulk material. *Nanoscale* **7**, 10421–10429 (2015).
49. Mak, K. F., Lee, C., Hone, J., Shan, J. & Heinz, T. F. Atomically thin MoS2: a new direct-gap semiconductor. *Phys. Rev. Lett.* **105**, 136805 (2010).
50. Terry, D. J. et al. Infrared-to-violet tunable optical activity in atomic films of GaSe, InSe, and their heterostructures. *2D Mater.* **5**, 041009 (2018).
51. Mudd, G. W. et al. The direct-to-indirect band gap crossover in two-dimensional van der Waals indium selenide crystals. *Sci. Rep.* **6**, 39619 (2016).
52. Tran, V., Soklaski, R., Liang, Y. & Yang, L. Layer-controlled band gap and anisotropic excitons in few-layer black phosphorus. *Phys. Rev. B* **89**, 235319 (2014).
53. Tian, R. et al. Observation of excitonic series in monolayer and few-layer black phosphorus. *Phys. Rev. B* **101**, 235407 (2020).
54. Qiao, J., Kong, X., Hu, Z.-X., Yang, F. & Ji, W. High-mobility transport anisotropy and linear dichroism in few-layer black phosphorus. *Nat. Commun.* **5**, 4475 (2014).
55. Ma, T., Lin, H.-Q. & Gubernatis, J. E. Triplet p+ip pairing correlations in the doped Kane-Mele-Hubbard model: a quantum Monte Carlo study. *EPL Europhys. Lett.* **111**, 47003 (2015).
56. Cao, Y. et al. Unconventional superconductivity in magic-angle graphene superlattices. *Nature* **556**, 43–50 (2018).
57. Brooks, J., Weng, G., Taylor, S. & Vlcek, V. Stochastic many-body perturbation theory for Moiré states in twisted bilayer phosphorene. *J. Phys. Condens. Matter* **32**, 234001 (2020).
58. Zhao, S. et al. Anisotropic moiré optical transitions in twisted monolayer/bilayer phosphorene heterostructures. *Nat. Commun.* **12**, 3947 (2021).
59. Yang, J. et al. Optical tuning of exciton and trion emissions in monolayer phosphorene. *Light Sci. Appl.* **4**, e312–e312 (2015).
60. Yoo, W. S., Kang, K., Murai, G. & Yoshimoto, M. Temperature dependence of photoluminescence spectra from crystalline silicon. *ECS J. Solid State Sci. Technol.* **4**, P456 (2015).
61. Pei, J. et al. Producing air-stable monolayers of phosphorene and their defect engineering. *Nat. Commun.* **7**, 10450 (2016).
62. Liu, H. et al. Phosphorene: an unexplored 2D semiconductor with a high hole mobility. *ACS Nano* **8**, 4033–4041 (2014).
63. Xu, R. et al. Extraordinarily bound quasi-one-dimensional trions in two-dimensional phosphorene atomic semiconductors. *ACS Nano* **10**, 2046–2053 (2016).
64. Sharma, A. et al. Defect engineering in few-layer phosphorene. *Small* **14**, 1704556 (2018).
65. Xu, R. et al. Layer-dependent surface potential of phosphorene and anisotropic/layer-dependent charge transfer in phosphorene–gold hybrid systems. *Nanoscale* **8**, 129–135 (2016).
66. Akhtar, M. et al. Recent advances in synthesis, properties, and applications of phosphorene. *Npj 2D Mater. Appl.* **1**, 1–13 (2017).
67. Chen, C. et al. Bright mid-infrared photoluminescence from thin-film black phosphorus. *Nano Lett.* **19**, 1488–1493 (2019).
68. Chaves, A., Ji, W., Maassen, J., Dumitrica, T. & Low, T. Theoretical overview of black phosphorus. Preprint at https://arxiv.org/abs/1710.05808 (2017). Published in Avouris, P., Heinz, T. F., Low, T. 2D Materials. Cambridge University Press (2017) (https://doi.org/10.1017/9781316681619.022).
69. Wang, G. et al. Colloquium: excitons in atomically thin transition metal dichalcogenides. *Rev. Mod. Phys.* **90**, 021001 (2018).
70. Koperski, M. et al. Optical properties of atomically thin transition metal dichalcogenides: observations and puzzles. *Nanophotonics* **6**, 1289–1308 (2017).
71. Molas, M. R. et al. Energy spectrum of two-dimensional excitons in a nonuniform dielectric medium. *Phys. Rev. Lett.* **123**, 136801 (2019).
72. Goryca, M. et al. Revealing exciton masses and dielectric properties of monolayer semiconductors with high magnetic fields. *Nat. Commun.* **10**, 4172 (2019).
73. Vaclavkova, D. et al. Singlet and triplet trions in WS2 monolayer encapsulated in hexagonal boron nitride. *Nanotechnology* **29**, 325705 (2018).
74. Wang, X. et al. Highly anisotropic and robust excitons in monolayer black phosphorus. *Nat. Nanotechnol.* **10**, 517–521 (2015).
75. Raja, A. et al. Coulomb engineering of the bandgap and excitons in two-dimensional materials. *Nat. Commun.* **8**, 15251 (2017).
76. MacDonald, A. H. & Ritchie, D. S. Hydrogenic energy levels in two dimensions at arbitrary magnetic fields. *Phys. Rev. B* **33**, 8336–8344 (1986).
77. Keldysh, L. V. Coulomb interaction in thin semiconductor and semimetal films. *Sov. J. Exp. Theor. Phys. Lett.* **29**, 658 (1979).
78. Stier, A. V. et al. Magnetooptics of exciton Rydberg states in a monolayer semiconductor. *Phys. Rev. Lett.* **120**, 057405 (2018).
79. Schindlmayr, A. Excitons with anisotropic effective mass. *Eur. J. Phys.* **18**, 374 (1997).
80. Chaves, A. et al. Anisotropic exciton Stark shift in black phosphorus. *Phys. Rev. B* **91**, 155311 (2015).
81. Chernikov, A. et al. Exciton binding energy and nonhydrogenic Rydberg series in monolayer WS(2). *Phys. Rev. Lett.* **113**, 076802 (2014).
82. Yoon, S. et al. Electrical control of anisotropic and tightly bound excitons in bilayer phosphorene. *Phys. Rev. B* **103**, L041407 (2021).
83. Guo, C.-L., Sun, C.-Z., Hao, Z.-B. & Luo, Y. Theoretical analysis of polarization insensitive InGaAsP multiple-quantum-wells eletroabsorption modulators with negative chirp. *Jpn. J. Appl. Phys.* **39**, 6166–6169 (2000).
84. Molas, M. R. et al. Tuning carrier concentration in a superacid treated MoS2 monolayer. *Sci. Rep.* **9**, 1989 (2019).
85. Kim, J. et al. Anomalous polarization dependence of Raman scattering and crystallographic orientation of black phosphorus. *Nanoscale* **7**, 18708–18715 (2015).
86. Freysoldt, C. et al. First-principles calculations for point defects in solids. *Rev. Mod. Phys.* **86**, 253–305 (2014).
87. Wu, Z. & Ni, Z. Spectroscopic investigation of defects in two-dimensional materials. *Nanophotonics* **6**, 1219–1237 (2017).
88. Hong, J. et al. Exploring atomic defects in molybdenum disulphide monolayers. *Nat. Commun.* **6**, 6293 (2015).
89. Huang, P. Y. et al. Grains and grain boundaries in single-layer graphene atomic patchwork quilts. *Nature* **469**, 389–392 (2011).
90. Kiraly, B., Hauptmann, N., Rudenko, A. N., Katsnelson, M. I. & Khajetoorians, A. A. Probing single vacancies in black phosphorus at the atomic level. *Nano Lett.* **17**, 3607–3612 (2017).

MOST WIEDZY Downloaded from mostwiedzy.pl

91. Kundu, S., Naik, M. H. & Jain, M. Native point defects in mono and bilayer phosphorene. *Phys. Rev. Mater.* **4**, 054004 (2020).
92. Liu, Y., Xu, F., Zhang, Z., Penev, E. S. & Yakobson, B. I. Two-dimensional mono-elemental semiconductor with electronically inactive defects: the case of phosphorus. *Nano Lett.* **14**, 6782–6786 (2014).
93. Banhart, F., Kotakoski, J. & Krasheninnikov, A. V. Structural defects in graphene. *ACS Nano* **5**, 26–41 (2011).
94. Najmaei, S. et al. Tailoring the physical properties of molybdenum disulfide monolayers by control of interfacial chemistry. *Nano Lett.* **14**, 1354–1361 (2014).
95. Sercombe, D. et al. Optical investigation of the natural electron doping in thin MoS2 films deposited on dielectric substrates. *Sci. Rep.* **3**, 3489 (2013).
96. Nan, H. et al. Strong photoluminescence enhancement of $MoS_2$ through defect engineering and oxygen bonding. *ACS Nano* **8**, 5738–5745 (2014).
97. Lin, Z. et al. Defect engineering of two-dimensional transition metal dichalcogenides. *2D Mater.* **3**, 022002 (2016).
98. Komsa, H. P. et al. Two-dimensional transition metal dichalcogenides under electron irradiation: defect production and doping. *Phys. Rev. Lett.* **109**, 035503 (2012).
99. Yang, X. L., Guo, S. H., Chan, F. T., Wong, K. W. & Ching, W. Y. Analytic solution of a two-dimensional hydrogen atom. I. Nonrelativistic theory. *Phys. Rev. A* **43**, 1186–1196 (1991).
100. Wang, J. et al. Recent progress on localized field enhanced two-dimensional material photodetectors from ultraviolet—visible to infrared. *Small* **13**, 1700894 (2017).
101. Hertel, T., Himmelein, S., Ackermann, T., Stich, D. & Crochet, J. Diffusion limited photoluminescence quantum yields in 1-D semiconductors: single-wall carbon nanotubes. *ACS Nano* **4**, 7161–7168 (2010).
102. Geim, A. K. & Grigorieva, I. V. Van der Waals heterostructures. *Nature* **499**, 419–425 (2013).
103. Kistanov, A. A., Cai, Y., Zhou, K., Dmitriev, S. V. & Zhang, Y.-W. The role of H2O and O2 molecules and phosphorus vacancies in the structure instability of phosphorene. *2D Mater.* **4**, 015010 (2016).
104. Utt, K. L. et al. Intrinsic defects, fluctuations of the local shape, and the photo-oxidation of black phosphorus. *ACS Cent. Sci.* **1**, 320–327 (2015).
105. Kuriakose, S. et al. Effects of plasma-treatment on the electrical and optoelectronic properties of layered black phosphorus. *Appl. Mater. Today* **12**, 244–249 (2018).
106. Illarionov, Y. Y. et al. Highly-stable black phosphorus field-effect transistors with low density of oxide traps. *Npj 2D Mater. Appl.* **1**, 1–7 (2017).
107. Fan, S. et al. Optical investigation of strong exciton localization in high Al composition AlxGa1-xN alloys. *Opt. Express* **21**, 24497–24503 (2013).
108. Cho, Y.-H. et al. "S-shaped" temperature-dependent emission shift and carrier dynamics in InGaN/GaN multiple quantum wells. *Appl. Phys. Lett.* **73**, 1370–1372 (1998).
109. Hong, C.-C., Ahn, H., Wu, C.-Y. & Gwo, S. Strong green photoluminescence from InxGa_1-xN/GaN nanorod arrays. *Opt. Express* **17**, 17227 (2009).
110. Xu, R. et al. Exciton brightening in monolayer phosphorene via dimensionality modification. *Adv. Mater.* **28**, 3493–3498 (2016).
111. Yuan, H. et al. Polarization-sensitive broadband photodetector using a black phosphorus vertical p–n junction. *Nat. Nanotechnol.* **10**, 707–713 (2015).
112. Zhang, W., Yin, J., Zhang, P. & Ding, Y. Strain/stress engineering on the mechanical and electronic properties of phosphorene nanosheets and nanotubes. *RSC Adv.* **7**, 51466–51474 (2017).
113. Maria, J. P., Bhuvaneswari, R., Nagarajan, V. & Chandiramouli, R. Surface adsorption studies of benzyl bromide and bromobenzyl cyanide vapours on black phosphorene nanosheets—a first-principles perception. *Mol. Phys.* **118**, e1737744 (2020).
114. Peng, X., Copple, A. & Wei, Q. Edge effects on the electronic properties of phosphorene nanoribbons. *J. Appl. Phys.* **116**, 144301 (2014).
115. Hao, F. & Chen, X. Mechanical properties of phosphorene nanoribbons and oxides. *J. Appl. Phys.* **118**, 234304 (2015).
116. Carvalho, A., Rodin, A. S. & Castro Neto, A. H. Phosphorene nanoribbons. *EPL Europhys. Lett.* **108**, 47005 (2014).
117. Guo, H., Lu, N., Dai, J., Wu, X. & Zeng, X. C. Phosphorene nanoribbons, phosphorus nanotubes, and van der Waals multilayers. *J. Phys. Chem. C* **118**, 14051–14059 (2014).
118. Guo, C., Wang, T., Xia, C. & Liu, Y. Modulation of electronic transport properties in armchair phosphorene nanoribbons by doping and edge passivation. *Sci. Rep.* **7**, 12799 (2017).
119. Wu, Q. et al. Electronic and transport properties of phosphorene nanoribbons. *Phys. Rev. B* **92**, 035436 (2015).
120. Yu, S. et al. A computational study of the electronic properties of one-dimensional armchair phosphorene nanotubes. *J. Appl. Phys.* **118**, 164306 (2015).
121. Allec, S. I. & Wong, B. M. Inconsistencies in the electronic properties of phosphorene nanotubes: new insights from large-scale DFT calculations. *J. Phys. Chem. Lett.* **7**, 4340–4345 (2016).
122. Ansari, R., Shahnazari, A. & Rouhi, S. A density-functional-theory-based finite element model to study the mechanical properties of zigzag phosphorene nanotubes. *Phys. E Low-Dimens. Syst. Nanostruct.* **88**, 272–278 (2017).
123. Fernández-Escamilla, H. N., Guerrero-Sánchez, J., Martínez-Guerra, E. & Takeuchi, N. Structural and electronic properties of double-walled black phosphorene nanotubes: a density functional theory study. *J. Phys. Chem. C* **123**, 7217–7224 (2019).
124. Zhang, X. et al. Black phosphorus quantum dots. *Angew. Chem. Int. Ed.* **54**, 3653–3657 (2015).
125. Lee, A.-Y. et al. Hybrid black phosphorus/zero-dimensional quantum dot phototransistors: tunable photodoping and enhanced photoresponsivity. *ACS Appl. Mater. Interfaces* **10**, 16033–16040 (2018).
126. Yuan, Y.-J. et al. Bandgap-tunable black phosphorus quantum dots: visible-light-active photocatalysts. *Chem. Commun.* **54**, 960–963 (2018).
127. Jing, Y., Tang, Q., He, P., Zhou, Z. & Shen, P. Small molecules make big differences: molecular doping effects on electronic and optical properties of phosphorene. *Nanotechnology* **26**, 095201 (2015).
128. Seixas, L., Rodin, A. S., Carvalho, A. & Castro Neto, A. H. Exciton binding energies and luminescence of phosphorene under pressure. *Phys. Rev. B* **91**, 115437 (2015).
129. San-Jose, P., Parente, V., Guinea, F., Roldán, R. & Prada, E. Inverse funnel effect of excitons in strained black phosphorus. *Phys. Rev. X* **6**, 031046 (2016).
130. Zhang, G. et al. Infrared fingerprints of few-layer black phosphorus. *Nat. Commun.* **8**, 14071 (2017).
131. Zhang, Z. et al. Strain-modulated bandgap and piezo-resistive effect in black phosphorus field-effect transistors. *Nano Lett.* **17**, 6097–6103 (2017).
132. Huang, S. et al. Strain-tunable van der Waals interactions in few-layer black phosphorus. *Nat. Commun.* **10**, 2447 (2019).
133. Qiu, D. Y., da Jornada, F. H. & Louie, S. G. Environmental screening effects in 2D materials: renormalization of the bandgap, electronic structure, and optical spectra of few-layer black phosphorus. *Nano Lett.* **17**, 4706–4712 (2017).
134. Chernikov, A. et al. Electrical tuning of exciton binding energies in monolayer WS2. *Phys. Rev. Lett.* **115**, 126802 (2015).
135. Liu, E. et al. Multipath optical recombination of intervalley dark excitons and trions in monolayer WSe2. *Phys. Rev. Lett.* **124**, 196802 (2020).
136. Surrente, A. et al. Excitons in atomically thin black phosphorus. *Phys. Rev. B* **93**, 121405 (2016).
137. Chen, C. et al. Widely tunable mid-infrared light emission in thin-film black phosphorus. *Sci. Adv.* **6**, eaay6134 (2020).
138. Rajapakse, M. et al. Intercalation as a versatile tool for fabrication, property tuning, and phase transitions in 2D materials. *Npj 2D Mater. Appl.* **5**, 1–21 (2021).
139. Wang, C. et al. Monolayer atomic crystal molecular superlattices. *Nature* **555**, 231–236 (2018).
140. Abellán, G. et al. Exploring the formation of black phosphorus intercalation compounds with alkali metals. *Angew. Chem. Int. Ed.* **56**, 15267–15273 (2017).
141. Zhang, R., Waters, J., Geim, A. K. & Grigorieva, I. V. Intercalant-independent transition temperature in superconducting black phosphorus. *Nat. Commun.* **8**, 15036 (2017).
142. Rajapakse, M. et al. Electrochemical Li intercalation in black phosphorus: in situ and ex situ studies. *J. Phys. Chem. C* **124**, 10710–10718 (2020).
143. Azizi, A. et al. Layer-dependent electronic structure of atomically resolved two-dimensional gallium selenide telluride. *Nano Lett.* **19**, 1782–1787 (2019).
144. Ma, Y., Dai, Y., Kou, L., Frauenheim, T. & Heine, T. Robust Two-dimensional topological insulators in methyl-functionalized bismuth, antimony, and lead bilayer films. *Nano Lett.* **15**, 1083–1089 (2015).
145. Jin, K.-H. & Jhi, S.-H. Quantum anomalous Hall and quantum spin-Hall phases in flattened Bi and Sb bilayers. *Sci. Rep.* **5**, 8426 (2015).
146. Kou, L. et al. Structural and electronic properties of layered arsenic and antimony arsenide. *J. Phys. Chem. C* **119**, 6918–6922 (2015).
147. Ezawa, M. A topological insulator and helical zero mode in silicene under an inhomogeneous electric field. *N. J. Phys.* **14**, 033003 (2012).
148. Wang, D., Chen, L., Liu, H. & Wang, X. Topological phase transitions in Sb(111) films driven by external strain and electric field. *EPL Europhys. Lett.* **104**, 57011 (2013).
149. Chen, Y. et al. Tunable band gap photoluminescence from atomically thin transition-metal dichalcogenide alloys. *ACS Nano* **7**, 4610–4616 (2013).
150. Zhao, N., Zhu, Y. F. & Jiang, Q. Novel electronic properties of two-dimensional $As_x$ $Sb_y$ alloys studied using DFT. *J. Mater. Chem. C* **6**, 2854–2861 (2018).
151. Zhu, Z., Guan, J. & Tománek, D. Structural transition in layered $As_{1-x}$ $P_x$ compounds: a computational study. *Nano Lett.* **15**, 6042–6046 (2015).
152. Zhu, Z. & Tománek, D. Semiconducting layered blue phosphorus: a computational study. *Phys. Rev. Lett.* **112**, 176802 (2014).
153. Osters, O. et al. Synthesis and identification of metastable compounds: black arsenic—science or fiction? *Angew. Chem. Int. Ed.* **51**, 2994–2997 (2012).
154. Sun, J. et al. The electronic structure, mechanical flexibility and carrier mobility of black arsenic–phosphorus monolayers: a first principles study. *Phys. Chem. Chem. Phys.* **18**, 9779–9787 (2016).

MOST WIEDZY Downloaded from mostwiedzy.pl

155. Ogilvie, S. P. et al. Considerations for spectroscopy of liquid-exfoliated 2D materials: emerging photoluminescence of N -methyl-2-pyrrolidone. *Sci. Rep.* **7**, 16706 (2017).
156. Snyder, L. R. Classification of the solvent properties of common liquids. *J. Chromatogr. A* **92**, 223–230 (1974).
157. Wang, K. et al. Donor–acceptor type black phosphorus nanosheets covalently functionalized with a conjugated polymer for laser protection. *Polym. Chem.* **10**, 6003–6009 (2019).
158. Wang, H. et al. Black phosphorus nanosheets passivation using a tripeptide. *Small* **14**, 1801701 (2018).
159. Kumar, A. Simultaneous passivation and encapsulation of black phosphorus nanosheets (phosphorene) by optically active polypeptide micelles for biosensors. *ACS Appl. Nano Mater.* **2**, 2397–2404 (2019).
160. Teng Yew, Y., Sofer, Z., C. Mayorga-Martinez, C. & Pumera, M. Black phosphorus nanoparticles as a novel fluorescent sensing platform for nucleic acid detection. *Mater. Chem. Front.* **1**, 1130–1136 (2017).
161. Gu, W. et al. Fluorescent black phosphorus quantum dots as label-free sensing probes for evaluation of acetylcholinesterase activity. *Sens. Actuators B Chem.* **250**, 601–607 (2017).
162. Vishnoi, P., Mazumder, M., Barua, M., Pati, S. K. & Rao, C. N. R. Phosphorene quantum dots. *Chem. Phys. Lett.* **699**, 223–228 (2018).
163. Jakóbczyk, P. et al. Low-power microwave-induced fabrication of functionalised few-layer black phosphorus electrodes: a novel route towards *Haemophilus influenzae* pathogen biosensing devices. *Appl. Surf. Sci.* **539**, 148286 (2021).
164. Li, L. et al. Direct observation of the layer-dependent electronic structure in phosphorene. *Nat. Nanotechnol.* **12**, 6 (2017).
165. Bhuvaneswari, R. & Chandiramouli, R. First-principles investigation on detection of phosgene gas molecules using phosphorene nanosheet device. *Chem. Phys. Lett.* **717**, 99–106 (2019).
166. Saroka, V. A., Lukyanchuk, I., Portnoi, M. E. & Abdelsalam, H. Electro-optical properties of phosphorene quantum dots. *Phys. Rev. B* **96**, 085436 (2017).
167. Liu, B. et al. Black arsenic–phosphorus: layered anisotropic infrared semiconductors with highly tunable compositions and properties. *Adv. Mater.* **27**, 4423–4429 (2015).
168. Marfoua, B. & Hong, J. Transport properties of 2D As1-xPx binary compounds as a potential thermoelectric materials. *Phys. E Low-Dimens. Syst. Nanostruct.* **111**, 79–83 (2019).
169. Cai, B. et al. A promising two-dimensional channel material: monolayer antimonide phosphorus. *Sci. China Mater.* **59**, 648–656 (2016).
170. Cao, Y. et al. Covalent functionalization of black phosphorus with conjugated polymer for information storage. *Angew. Chem. Int. Ed.* **57**, 4543–4548 (2018).
171. Cao, Y., Zhang, B., Tian, X., Gu, M. & Chen, Y. Direct covalent modification of black phosphorus quantum dots with conjugated polymers for information storage. *Nanoscale* **11**, 3527–3533 (2019).
172. Meng, X. et al. Photoluminescence lifetime of black phosphorus nanoparticles and their applications in live cell imaging. *ACS Appl. Mater. Interfaces* **10**, 31136–31145 (2018).
173. Xu, Y. et al. Cholesterol-modified black phosphorus nanospheres for the first NIR-II fluorescence bioimaging. *ACS Appl. Mater. Interfaces* **11**, 21399–21407 (2019).
174. Zhao, Y. et al. Stable and multifunctional dye-modified black phosphorus nanosheets for near-infrared imaging-guided photothermal therapy. *Chem. Mater.* **29**, 7131–7139 (2017).
175. Wu, L. et al. Lanthanide-coordinated black phosphorus. *Small* **14**, 1801405 (2018).
176. Fan, S. et al. Solution-based property tuning of black phosphorus. *ACS Appl. Mater. Interfaces* **10**, 39890–39897 (2018).

## ACKNOWLEDGEMENTS

Ł.M., P.J., and R.B. were supported by the Polish National Science Centre [2016/22/E/ST7/00102]. M.R.M. acknowledges support from the National Science Centre, Poland (2018/31/B/ST3/02111). J.B.J. was supported by the U.S. Department of Energy, Office of Science, Basic Energy Sciences, under Award # DE-SC0019348.

## AUTHOR CONTRIBUTIONS

R.B., J.B.J., and M.R.M. conceived the outline of the review and directed the overall project, including organizing all contributions and editing the manuscript. All authors contributed to literature search, writing of the "Abstract" and "Introduction" and "Summary and outlook," and preparation of the figures. In addition, M.R.M., J.B.J., Ł.M., and A.W. contributed to "PL and optical bandgap of BP" and "Bandgap engineering iN BP" and P.J. contributed to "Bandgap engineering iN BP". All authors have given approval to the final version of the manuscript.

## COMPETING INTERESTS

The authors declare no competing interests.

## ADDITIONAL INFORMATION

**Correspondence** and requests for materials should be addressed to Robert Bogdanowicz or Jacek B. Jasinski.

**Reprints and permission information** is available at http://www.nature.com/reprints

**Publisher's note** Springer Nature remains neutral with regard to jurisdictional claims in published maps and institutional affiliations.

**Open Access** This article is licensed under a Creative Commons Attribution 4.0 International License, which permits use, sharing, adaptation, distribution and reproduction in any medium or format, as long as you give appropriate credit to the original author(s) and the source, provide a link to the Creative Commons license, and indicate if changes were made. The images or other third party material in this article are included in the article's Creative Commons license, unless indicated otherwise in a credit line to the material. If material is not included in the article's Creative Commons license and your intended use is not permitted by statutory regulation or exceeds the permitted use, you will need to obtain permission directly from the copyright holder. To view a copy of this license, visit http://creativecommons.org/licenses/by/4.0/.

© The Author(s) 2021

MOST WIEDZY Downloaded from mostwiedzy.pl